Gapless spin liquid behavior in a kagome Heisenberg antiferromagnet with randomly distributed hexagons of alternate bonds

Jiabin Liu,[1,*] Long Yuan,[1,*] Xuan Li,[2,3,*] Boqiang Li,[1] Kan Zhao,[4] Haijun Liao,[2,5,†] and Yuesheng Li[1,‡]

[1]*Wuhan National High Magnetic Field Center and School of Physics, Huazhong University of Science and Technology, 430074 Wuhan, China*

[2]*Institute of Physics, Chinese Academy of Sciences, P.O. Box 603, Beijing 100190, China*

[3]*University of Chinese Academy of Sciences, Beijing 100049, China*

[4]*School of Physics, Beihang University, Beijing 100191, China*

[5]*Songshan Lake Materials Laboratory, Dongguan, Guangdong 523808, China*

(Received 26 July 2021; revised 4 January 2022; accepted 10 January 2022; published 18 January 2022)

We demonstrate that the single crystal of $YCu_3[OH(D)]_{6.5}Br_{2.5}$ (YCOB) is a kagome Heisenberg antiferromagnet without evident orphan spins ($\ll 0.8\%$). The site mixing between polar OH^- and nonpolar Br^- causes local distortions of Cu–O–Cu exchange paths and gives rise to 70(2)% of randomly distributed hexagons of alternate bonds ($\sim J_1 - \Delta J$ and $J_1 + \Delta J$) and the rest of the almost-uniform hexagons ($\sim J_1$) on the kagome lattice. Simulations of the random exchange model with $\Delta J/J_1 = 0.7(1)$ show good agreement with experimental observations, including the weak upturn seen in susceptibility and the slight polarization in magnetization. Despite the average antiferromagnetic coupling of $J_1 \sim 60$ K, no conventional freezing is observed down to $T \sim 0.001J_1$, and the raw specific heat exhibits a nearly quadratic temperature dependence below 1 K $\sim 0.02J_1$, phenomenologically consistent with a gapless (spin gap $\leqslant 0.025J_1$) Dirac quantum spin liquid (QSL). Our result sheds light on the theoretical understanding of the randomness-relevant gapless QSL behavior in YCOB, as well as in other relevant materials.

DOI: 10.1103/PhysRevB.105.024418

I. INTRODUCTION

The search for quantum spin liquid (QSL) has become one of the central topics in the fields spanning experiment and theory since Anderson's initial proposal [1]. QSLs are intimately related to the realization of topological quantum computation [2] and the understanding of high-temperature superconductivity [3] due to exotic fractional excitations [4] and other emergent properties [5–8]. The $S = \frac{1}{2}$ kagome Heisenberg antiferromagnet (KHA) [9–17] is one of the most promising candidates hosting QSLs. Despite recent progress, the precise nature of QSL in the KHA remains elusive. Previous density-matrix renormalization group (DMRG) studies imply a fully gapped $\mathbb{Z}_2$ QSL ground state (GS) [16,17], but variational Monte Carlo [11,18,19], tensor network [12], and more recent DMRG [13] calculations suggest a gapless Dirac QSL.

Experimentally, many prominent $S = \frac{1}{2}$ KHAs have been extensively studied, including $ZnCu_3(OH)_6Cl_2$ (herbertsmithite) [20–28], α-$Cu_3Zn(OH)_6Cl_2$ (kapellasite) [29,30], $Cu_3Zn(OH)_6FBr$ [31,32], $[NH_4]_2[C_7H_{14}N][V_7O_6F_{18}]$ [33,34], $(CH_3NH_3)_2NaTi_3F_{12}$ [35], $ZnCu_3(OH)_6SO_4$ [36–38], etc. They show no conventional magnetic transitions down to the lowest measuring temperature despite the strong exchange couplings. However, most of these candidates suffer from 4–27% of magnetic defects [25,28,30,31,34–36]. Orphan spins created by these magnetic defects contribute a pronounced Curie-like tail of magnetic susceptibility [22,34] and Schottky-like anomaly of specific heat [23,34] at low temperatures ($\leqslant$100 K), and thus prevent us from probing the intrinsic low-energy properties [39]. Therefore, achieving ultrahigh-quality materials is still the key challenge for the study of kagome QSLs [6].

Recently, a kagome QSL candidate, nondeuterated $YCu_3(OH)_{6.5}Br_{2.5}$, had been successfully synthesized [40] by Chen *et al.* The magnetic Cu^{2+} ($S = \frac{1}{2}$) ions were expected to fully occupy the regular kagome sites and be free from the site mixing with other nonmagnetic ions [40]. Despite the strong antiferromagnetic coupling, $YCu_3[OH(D)]_{6.5}Br_{2.5}$ (YCOB) exhibits no magnetic transition down to 50 mK [40,41]. However, the low-energy magnetism of this promising QSL candidate YCOB remains poorly understood.

In this paper, we report a comprehensive study of the frustrated magnetism on a high-quality single crystal of YCOB, including subkelvin thermodynamic and electron spin resonance (ESR) measurements and microscopic modeling by density functional theory (DFT) and state-of-the-art quantum many-body computations. The nonsymmetric distribution of OH^-/Br^- pushes 70(2)% of Y^{3+} away from its ideal position, and gives rise to two alternate local distortions of the Cu–O–Cu superexchange paths ($\sim J_1 - \Delta J$ and $J_1 + \Delta J$) around the hexagons on the kagome lattice, whereas the rest of symmetric local environments result in nearly uniform hexagons ($\sim J_1$). Through fitting the magnetic susceptibilities, we find a profound fluctuation of the exchange couplings, $\Delta J/J_1 \sim 0.7$. The weak upturn in the low-T susceptibility and the slight polarization in magnetization originate from the local

*These authors contributed equally to this paper.

†navyphysics@iphy.ac.cn

‡yuesheng_li@hust.edu.cn

moments induced by the bond randomness. Despite the average antiferromagnetic interaction of $J_1 \sim 60$ K, no magnetic freezing is found down to 50 mK [41] $\sim 0.001J_1$. Below $\sim 0.02J_1$, the specific heat exhibits a nearly quadratic temperature dependence, which is phenomenologically consistent with the predictions of a gapless U(1) Dirac QSL or a $\mathbb{Z}_2$ QSL with a gap less than $0.025J_1$. We argue that the bond randomness is a critical ingredient for the gapless QSL behavior observed in YCOB, as well as in other relevant materials.

II. EXPERIMENTAL DETAILS

We performed a recrystallization in a temperature gradient of $\sim 2\,^{\circ}$C/cm for a month, and obtained transparent green single crystals of YCOB (typical size $3 \times 3 \times 0.3$ mm) (see Appendix A). Magnetization up to 14 T and dc/ac susceptibilities down to 1.8 K were measured in a physical property measurement system (PPMS) and a magnetic property measurement system, respectively. The specific heat down to 0.36 K [42] was measured in a PPMS using a ^{3}He refrigerator. The ESR spectra were measured on continuous wave spectrometers at x-band frequencies ($\sim$9.7 GHz).

The DFT + U calculations were performed in the VIENNA AB INITIO SIMULATION PACKAGE (VASP) [43,44] (see Appendix B). We carried out the finite-temperature Lanczos diagonalization (FLD) simulations for the thermodynamic properties of YCOB, as well as the local susceptibility $\chi_i^{\rm loc}$ and correlation function. The FLD calculations were conducted on the 18-, 21-, 24-, and 27-site KHA clusters with periodic boundary conditions (PBCs), we excluded the thermodynamic data calculated below $T_{\rm min}$ in the main text, where the finite-size effect is significant (see Appendix C). We fit the experimental data by minimizing the residual function,

$$R_p = \sqrt{\frac{1}{N_0}\sum_i \left(\frac{X_i^{\rm obs} - X_i^{\rm cal}}{\sigma_i^{\rm obs}}\right)^2}, \qquad (1)$$

where N_0, $X_i^{\rm obs}$, and $\sigma_i^{\rm obs}$ are the number of the data points, the observed value, and its standard deviation, respectively, whereas $X_i^{\rm cal}$ is the calculated value. The international system of units is used throughout this paper.

III. RESULTS AND DISCUSSION

A. Exchange Hamiltonian

Figure 1(a) shows the crystal structure of YCOB, where the magnetic Cu^{2+} ($S = \frac{1}{2}$) ions occupy the $3f$ Wyckoff position of space group $P\bar{3}m1$ and form the kagome lattice [see Fig. 1(d)]. The site mixing between the magnetic Cu^{2+} (ionic radius $r_{Cu^{2+}} = 0.73$ Å) and other nonmagnetic ions, i.e., Y^{3+} ($r_{Y^{3+}} = 0.90$ Å), $H(D)^+$, O^{2-}, Br^-, is unlikely due to the large chemical differences, which has been confirmed by single-crystal x-ray diffraction (XRD) [40,41].

From the Curie-Weiss fitting, we get the Curie-Weiss temperatures $\theta_\perp = -57.5(4)$ K and $\theta_\parallel = -58.7(3)$ K (see Figs. 3 and 7), which indicate a strong antiferromagnetic exchange coupling, $J_1 \sim 60$ K [40]. A weak upturn is found in the susceptibilities below $\sim$30 K $\sim 0.5J_1$ [see Figs. 1(e) and 1(f)], which speaks against the simplest nearest-neighbor

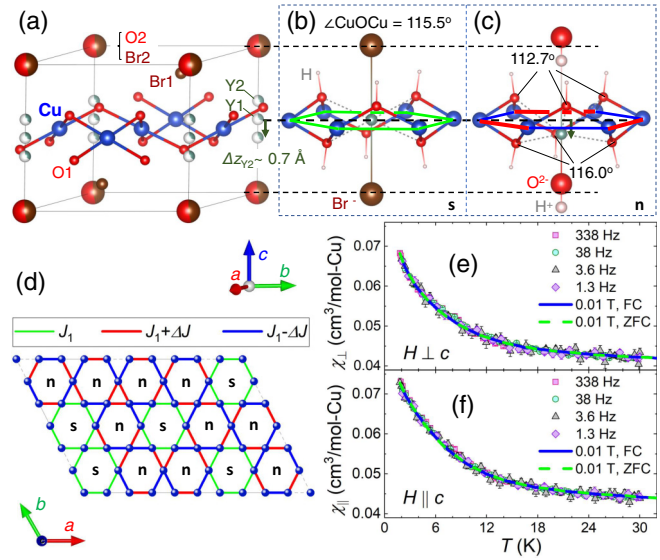

FIG. 1. (a) The experimental lattice structure of YCOB. (b), (c) Optimized crystal structures for supercells containing symmetric (s) and nonsymmetric (n) environments, respectively. The nonsymmetric environments (probability $\sim$70%) cause the deviations of Y^{3+} from its ideal positions (green arrows) and the alternate superexchanges [alternate ∠CuOCu are marked in (c)] along the hexagons on the kagome lattice of Cu^{2+}. (d) Sketch of model No. 2 with $\sim$30% of uniform hexagons (green) and $\sim$70% of randomly distributed hexagons of alternate bonds (blue and red). Real part of the ac susceptibilities measured on YCOB along the *ab* plane (e) and *c* axis (f), respectively. The dashed and solid lines present the dc susceptibilities measured at 0.01 T under zero-field cooling (ZFC) and field cooling (FC), respectively.

(NN) KHA model (see Fig. 3) [45] and suggests the existence of net magnetic moments. Unlike many other kagome QSL candidates [22,36], e.g., $ZnCu_3(OH)_6Cl_2$, the model of conventional orphan spins fails to explain all the low-T thermodynamic observations (see Fig. 2), which suggests the concentration of orphan spins is much lower than 0.8% in YCOB (see Appendix C). Therefore, the low-T behaviors are governed by the intrinsic properties of the specific KHA of YCOB, which deviates from the ideal NN KHA.

To understand the frustrated magnetism of the KHA YCOB, we consider the following spin-1/2 Hamiltonian in an applied magnetic field of **H**:

$$\mathcal{H} = \sum_{\langle ij \rangle} J_{1,ij}\mathbf{S}_i \cdot \mathbf{S}_j - \mu_0\mu_{\rm B}\mathbf{H}\cdot\mathbf{g}\cdot\sum_i \mathbf{S}_i + \mathcal{H}', \qquad (2)$$

where $\mathbf{g}$ is the diagonal matrix of g factor with $g_\perp = 2.18(1)$ and $g_\parallel = 2.19(1)$ determined by fitting the magnetic susceptibility data (see Fig. 3) and $\mathcal{H}'$ represents symmetry-allowed perturbations, including the Dzyaloshinsky-Moriya (DM) interaction [46,47], further-neighbor couplings [48], XXZ anisotropy [49], etc.

Starting with the simplest NN KHA (see Fig. 3 for model No. 1), we fit the magnetic susceptibilities ($\chi_\perp$ and $\chi_\parallel$) measured on YCOB above $\sim 0.1J_1 \sim 7$ K, and find $J_1 = 61.6$ K with the least $R_p \sim 3.3$ [50]. However, the weak upturn of $\chi_\perp$ and $\chi_\parallel$ below $\sim$30 K is poorly understood (see Fig. 3).

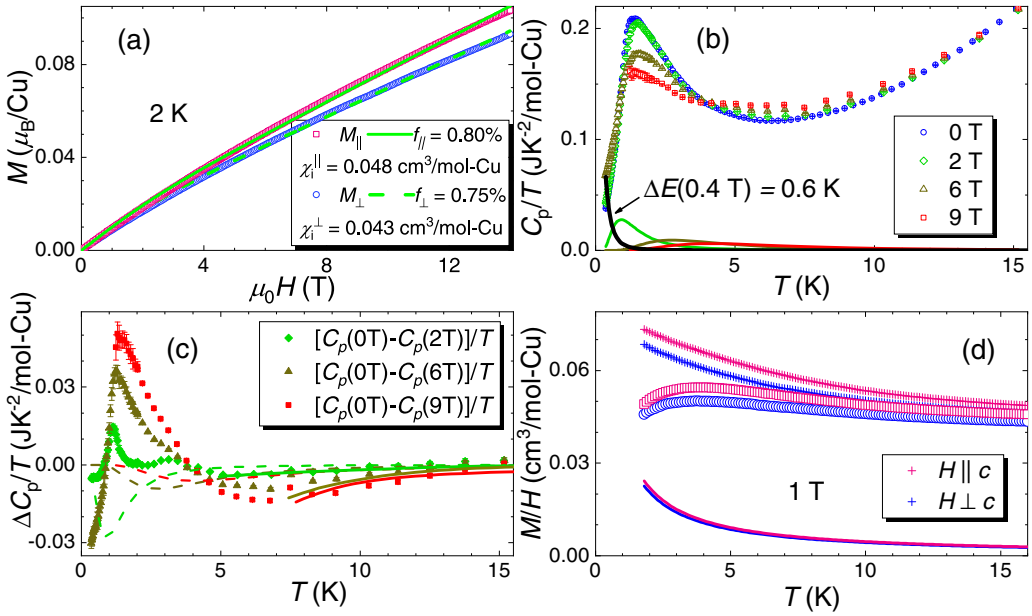

FIG. 2. (a) Magnetization measured at 2 K on the YCOB single crystal with the magnetic fields applied parallel and perpendicular to the c axis. The green lines present the Brillouin fits [see Eq. (C1)]. (b) Raw specific heat of YCOB measured in selected magnetic fields applied along the c axis, with the lines showing the calculated Schottky functions for 0.8% of free spins [see Eq. (C2)]. (c) The difference between the zero- and nonzero-field specific heat. The dashed lines show the calculations of 0.8% of free spins, whereas the solid lines present the 21-site FLD calculations of the random model No. 2 that is valid above $\sim 0.1J_1 \sim 7$ K. (d) Magnetic susceptibilities of YCOB measured at 1 T applied along the ab plane and c axis (cross). The hollow scatters show the data obtained by subtracting the Brillouin functions for 0.75% and 0.80% of free spins (colored lines) from the corresponding raw susceptibilities.

The measured magnetic anisotropy, $\chi_\parallel/\chi_\perp$, only increases by $\sim$4% from $T \sim J_1$ down to 1.8 K $\sim 0.03J_1$ [see the lower inset of Fig. 3(b)], suggesting that the interaction anisotropy isn't critical in YCOB due to the weak spin-orbit coupling of the $3d$ electrons. Based on the DFT+U calculation, we find that both further-neighbor and inter-layer exchange couplings are negligible, which are less than 4% of J_1 (highly similar to the sibling $YCu_3(OH)_6Cl_3$ [47]). Therefore, we mainly restrict ourselves to the effective models with only NN Heisenberg couplings at this stage.

In YCOB, the site mixing between OH^- and Br^- occurs around the ideal Y^{3+} site (Wyckoff position 1b at the center of each hexagon on the kagome lattice of Cu^{2+}) based on the XRD [40,41]. Although OH^- and Br^- have the same net charge, OH^- is polar, and causes local distortions that may have a strong influence on the exchange couplings. To go beyond the average structure from XRD, we performed the DFT calculations by constructing various OH/Br configurations (with H) to simulate this site-mixing effect. In the symmetric (e.g., Br–Br) configurations, the center of inversion is located at 1b [see Fig. 1(b)], and Y^{3+} occupies its ideal position with a statistical probability $f_{Y1} = 30(2)\%$ from XRD (see Table I) [40]. In contrast, the other nonsymmetric OH/Br configurations, e.g., OH–OH, push Y^{3+} away from its ideal position, $\Delta z_{Y2} \sim 0.1c \sim 0.6$ Å, well consistent with the XRD result [see Figs. 1(a) and 1(c)]. More importantly, the nonsymmetric configurations give rise to the alternate bond angles $\angle$CuOCu along the hexagons of the kagome lattice [see Fig. 1(c)]. Therefore, $1 - f_{Y1} = 70(2)\%$ of randomly distributed hexagons with alternate bonds ($\sim J_1 - \Delta J$ and $J_1 + \Delta J$) should be expected on the kagome lattice of YCOB [see Fig. 1(d)] [51].

We further conduct the DFT + U calculation to estimate the exchange couplings for YCOB and find that the fluctuation of these alternate bonds, $\Delta J/J_1$, is strong, ranging from 0 to $\sim$1.3 (see Appendix B). According to the simplified model of the crystal structure [see Fig. 1(a)], we construct a simple KHA model (No. 2) with $1 - f_{Y1} = 70\%$ of randomly distributed hexagons of alternate bonds and the rest of the almost uniform hexagons on the kagome lattice, as illustrated in Fig. 1(d). The real situation of YCOB may be more complicated, but one always seeks to explain the bulk of experimental observations within the minimum model that captures the essential physics.

Using model No. 2, we are able to fit the experimental susceptibilities very well at $J_1 = 50(1)$ K and $\Delta J/J_1 = 0.7(1)$ with a significantly reduced $R_p = 1.4(1)$ (see Fig. 3). The finite-size effect is trivial in model No. 2 [see Figs. 3 and 4(b)], and both the weak upturn below $\sim 0.5J_1$ and the broad hump at $\sim J_1$ can be excellently reproduced. In contrast, the bond-independent randomness of J_1 and g with a continuous Lorentzian distribution [52,53] fails to fit the experimental susceptibilities (see Fig. 13). Besides that, model No. 2 also well simulates the slight polarization seen in the low-T magnetization without any parameter tuning [the upper inset of Fig. 3(b)]. These observations strongly support the formation of effective $\sim$0.8% (see Fig. 2) of local moments due to the bond randomness (see Fig. 5) [54–57]. The temperature dependence of the ESR intensity shows a Curie-Weiss

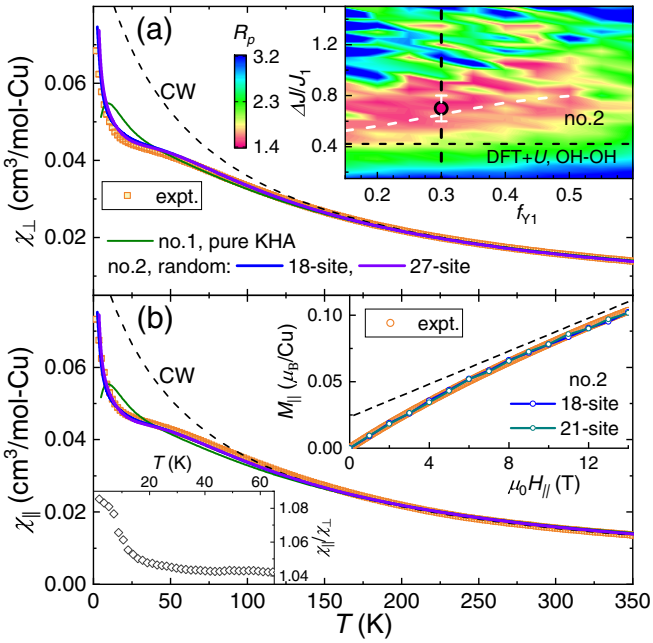

FIG. 3. Combined fits to the raw susceptibilities measured on YCOB along the *ab* plane (a) and *c* axis (b), respectively, using models No. 1 (ideal KHA) and No. 2 (with randomly distributed hexagons of alternate bonds). The dashed lines show the Curie-Weiss fits above 150 K. The inset of (a) presents the deviation R_p of using model No. 2, with the dotted white line showing the optimized parameters. The vertical dashed line presents the occupancy fraction of Y1 from XRD, $f_{Y1} = 0.30(2)$, and the horizontal line displays the bond randomness ($\Delta J/J_1$) calculated by DFT + U in the OH–OH configuration [Fig. 1(c)]. The circle shows the optimized value, $\Delta J/J_1 = 0.7(1)$. The upper inset of (b) presents the magnetization measured at 2 K, showing the 18- and 21-site FLD calculations of model No. 2. The dashed straight line marks a linear dependence. The lower inset of (b) displays the measured magnetic anisotropy ($\chi_{||}/\chi_\perp$).

behavior with the Curie-Weiss temperatures, $\theta_\perp^{\rm ESR} = -12(2)$ K and $\theta_{||}^{\rm ESR} = -16(4)$ K [Figs. 4(a) and 9(d)], suggesting the ESR lines may originate from the nearly free local moments induced by the bond randomness [58]. Moreover, the ESR spectra of YCOB are so narrow that the hyperfine structures are clearly visible (see Fig. 8), implying that the weak coupling between the randomness-induced moments may be nearly isotropic [46].

It is worth noting that the nearly free local moments induced by bond randomness in YCOB are from the nontrivial many-body correlations and random-singlet physics (see Fig. 5) [54,57–59], which is essentially different from the trivial orphan spins observed in other existing kagome QSL candidate materials. Above $0.02J_1 \sim 1$ K, the theory of the scaling collapse recently proposed by Kimchi *et al.* [60] is applicable to YCOB, confirming the formation of a random-singlet state. However, below ∼1 K the raw zero-field specific heat shows a power-law behavior $C_{\rm p} \propto T^\alpha$ with $\alpha = 2.31(1) > 1$ [Fig. 4(c)] and the existing theories obviously fail (see Fig. 16).

B. Sub-Kelvin specific heat and mean-field ansatz

Below ∼2 K, the lattice contribution is completely negligible [see Figs. 14(a) and 14(b)] in the Mott insulator YCOB with room-T resistance larger than 20 MΩ parallel and perpendicular to the *c* axis, and thus the raw specific heat directly measures the intrinsic magnetic properties that are sensitive to the low-energy ($\leqslant 3\%J_1$) density of states.

Despite the strong antiferromagnetic exchange coupling of $J_1 \sim 60$ K, no conventional magnetic freezing is evidenced, as there is neither splitting of zero-field-cooling and field-cooling dc susceptibilities nor frequency dependence of the ac susceptibilities down to 1.8 K ($\sim 0.03J_1$) [see Figs. 1(e) and 1(f)] [40]. No sharp λ specific heat peak was observed down to 0.36 K ($\sim 0.006J_1$) [see Fig. 4(c)]. Moreover, our recent thermal conductivity measurements show no sign of phase transitions down to ∼80 mK [61]. These observations consistently show that YCOB is a very promising (randomness-induced) QSL candidate without evident orphan spins, and thus one is able to explore in depth its intrinsic GS nature. Thereby, we analyze the experimental results by using the three most promising mean-field QSLs classified by the projective symmetry group method [11,62,63], including the uniform resonating valence bond (RVB) [11], U(1) Dirac [11], and $\mathbb{Z}_2[0,\pi]\beta$ [63] states.

The inherent exchange randomness should influence the GS nature of the spin system of YCOB. In contrast to the ideal KHA, the simulated GS of the random model indeed exhibits the signature of random-singlet or valence bond glass phases [56,57]. The pair of NN spins with strong exchange interaction ($J_1 + \Delta J$) tends to form a singlet with extremely strong local correlation $\langle \boldsymbol{S}_i \cdot \boldsymbol{S}_j \rangle \sim -0.7$ (see Fig. 5). However, the fraction of such singlets is still very low due to the strong frustration of the kagome lattice [58], even in the presence of strong exchange randomness [see Fig. 5(a)]. Therefore, the picture of mobile spinons is still applicable [57] and the mean-field asnsatz can nevertheless serve as a simple and phenomenological model for understanding the complicated GS nature of YCOB, despite the possible distribution of hopping strength (not as a direct function of the detailed distribution of the exchange couplings, see Fig. 5). The distribution of hopping strength due to bond randomness might be general in almost all of the well-studied spin-liquid candidate compounds, κ-$(ET)_2Cu_2(CN)_3$, $EtMe_3Sb[Pd(dmit)_2]_2$, $ZnCu_3(OH)_6Cl_2$, etc. [58].

The uniform RVB state gives rise to a linear temperature dependence of specific heat that obviously contradicts the observations in YCOB [see Fig. 17(d)]. The zero-field specific heat of YCOB shows a nearly quadratic behavior [see Fig. 4(c)], $C_{\rm p} \sim \gamma_2 T^2$ with $\gamma_2 = 0.11(1)$ JK^{-3}/mol-Cu, which is consistent with the U(1) Dirac state [11], with the NN hopping parameter $\chi_1 = \frac{k_{\rm B}}{J_1}\sqrt{\frac{6\sqrt{3}\zeta(3)R}{\pi\gamma_2}} = 0.29(1)$ and the Fermi velocity $v_{\rm F} = \frac{aJ_1\chi_1}{\sqrt{2}\hbar} = 1.07(5)\times 10^3$ m/s [11]. The resulting χ_1 is slightly larger than the self-consistent mean-field value 0.221 [64]. The mean-field (MF) theory fails to strictly impose the single-occupancy constraint [7,65], and the unphysical states may result in the overestimated coefficient γ_2(MF) = 0.188 JK^{-3}/mol-Cu. This failure gets more severe when a magnetic field is applied (see below).

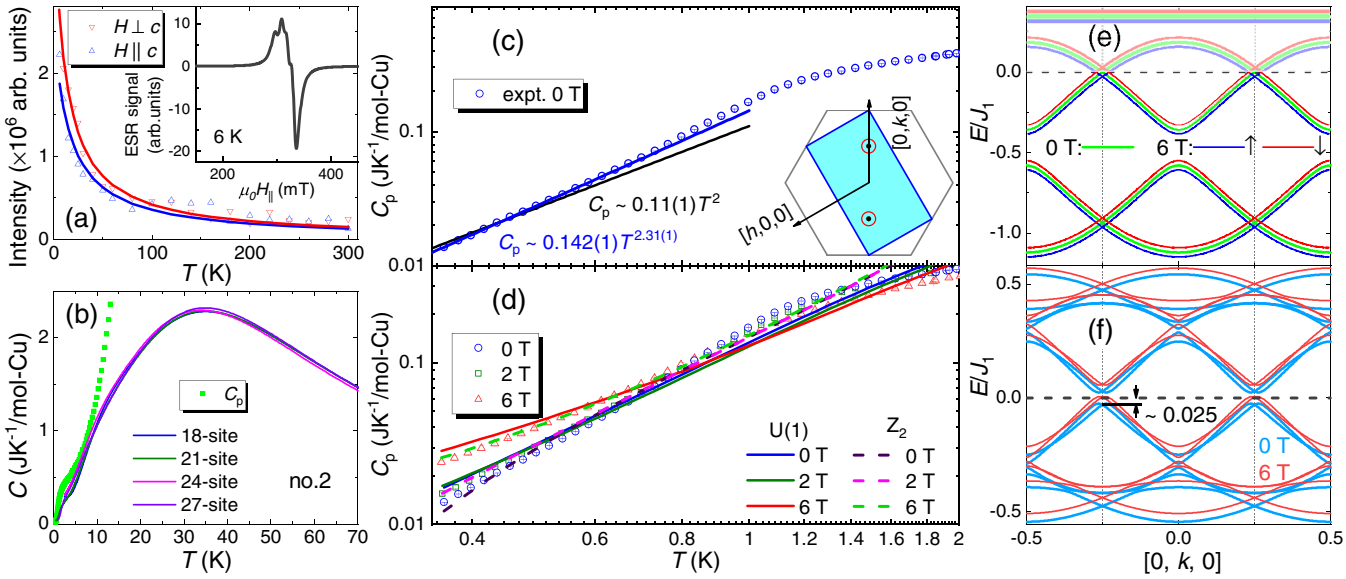

FIG. 4. (a) ESR intensities of YCOB. The color lines present the Curie-Weiss fits and the inset shows the ESR spectrum measured at 6 K along the c axis. (b) Magnetic specific heat calculated by using model No. 2 ($\Delta J/J_1 = 0.7$) on various size KHA clusters, with the experimental total specific heat for comparison. (c) Raw specific heat of YCOB measured at 0 T. The blue and black lines present the power-law and quadratic behaviors, respectively. The inset shows the Brillouin zone of the mean-field ansatz on the kagome lattice and the circles mark the positions of the Dirac nodes. (d) Raw specific heat measured in selected magnetic fields applied along the c axis. The thin and thick lines display the fittings below 1 K, using the U(1) and $\mathbb{Z}_2$ mean-field ansatz, respectively. (e) Band structure of the U(1) Dirac QSL at $h = 0$. The field of 6 T splits the zero-field bands (green) into the spin-up (↑, blue) and spin-down (↓, red) bands. (f) Band structure of the $\mathbb{Z}_2[0, \pi]\beta$ QSL in the Nambu representation at $h = 0$. The zero-field spin gap is marked.

TABLE I. Structure refinements from single-crystal XRD data measured on selected YCH and YCD crystals at 300 K.

Crystals	YCH (No. 1)	YCH (No. 2)	YCD (No. 1)	YCD (No. 2)
Size (mm)	0.22 × 0.22 × 0.08	0.19 × 0.19 × 0.08	0.21 × 0.21 × 0.04	0.11 × 0.11 × 0.06
Molar mass (g/mol)	588.0(1.3)	586.8(1.3)	589.5(1.3)	590.7(1.3)
Space group	$P\bar{3}m1$ (No. 164)	$P\bar{3}m1$ (No. 164)	$P\bar{3}m1$ (No. 164)	$P\bar{3}m1$ (No. 164)
a (= b, Å)	6.6647(3)	6.6704(5)	6.6576(4)	6.667(1)
c (Å)	6.0093(3)	6.0014(4)	6.0151(3)	6.004(1)
Cell volume (Å^3), $Z = 1$	231.16(3)	231.26(5)	230.89(4)	231.1(1)
Y1 (1b): occupancy f_{Y1}	0.30(2)	0.30(2)	0.30(2)	0.30(2)
$100\times U_{iso}$	0.8(2)	1.4(2)	0.9(2)	0.4(2)
Y2 (2c): occupancy f_{Y2}	0.35(1)	0.35(1)	0.35(1)	0.35(1)
z	0.374(2)	0.374(2)	0.373(2)	0.373(2)
$100\times U_{iso}$	0.8(2)	1.4(2)	0.9(2)	0.4(2)
Cu (3f, occupancy = 1): 100^*U_{iso}	0.8(1)	1.7(1)	0.8(1)	0.3(1)
Br1 (2d, occupancy = 1): z	0.8566(6)	0.8566(6)	0.8560(5)	0.8566(7)
$100\times U_{iso}$	1.8(1)	2.6(1)	1.8(1)	1.4(1)
O1 (6i, occupancy = 1): x ($x = 0.5y$)	0.1896(9)	0.1885(9)	0.1894(8)	0.189(1)
z	0.372(3)	0.362(2)	0.366(2)	0.378(3)
$100\times U_{iso}$	1.0(3)	1.4(4)	1.0(3)	1.5(5)
Br2 (1a): occupancy f_{Br2}	0.47(2)	0.45(2)	0.43(2)	0.45(2)
$100\times U_{iso}$	2.3(2)	2.8(4)	2.5(3)	1.6(4)
O2 (1a): occupancy f_{O2}	0.53(2)	0.55(2)	0.57(2)	0.55(2)
$100\times U_{iso}$	2.3(2)	2.8(4)	2.5(3)	1.6(4)
h range	$-9 \rightarrow 9$	$-9 \rightarrow 9$	$-8 \rightarrow 9$	$-7 \rightarrow 8$
k range	$-8 \rightarrow 11$	$-8 \rightarrow 11$	$-9 \rightarrow 11$	$-9 \rightarrow 11$
l range	$-8 \rightarrow 10$	$-3 \rightarrow 10$	$-8 \rightarrow 10$	$-8 \rightarrow 10$
Reflections ($I > 0$)	954	795	841	560
Reflections [$I > 3\sigma(I)$]	837	674	740	492
$R(F)$ [$I > 3\sigma(I)$]	3.8%	6.7%	7.1%	9.7%
$R_w(F)$ [$I > 3\sigma(I)$]	3.3%	4.8%	6.1%	6.6%

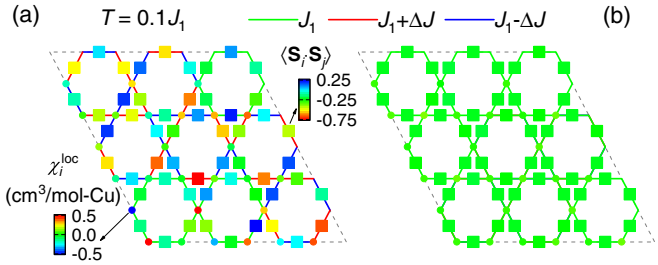

FIG. 5. Local susceptibility at each kagome site (see Ref. [55] for the definition) and correlation functions calculated for the 27-site samples of model No. 2 with bond randomness (a) and the ideal KHA model No. 1 (b), at $T = 0.1J_1$[a] and $\mu_0 H = 0$ T. The dashed lines display the cluster with PBCs.

[a]$T = 0.1J_1$ is low enough, as the correlation functions of both systems are nearly constant.

For the U(1) Dirac state, the applied magnetic field tends to form Fermi pockets [see Fig. 4(e)], increasing the low-energy density of states and thus low-T specific heat, which qualitatively accounts for the observations [see Fig. 4(d)]. However, the fermionic spinon with the effective magnetic moment $\mu_{\rm eff} \sim \mu_{\rm B}$ causes a much stronger dependence on the field in the mean-field theory, and can't fit well the specific heat measured in nonzero fields below $\sim$1 K [see Fig. 17(h)]. A remedy is to set $\mu_{\rm eff}$ as an adjustable parameter, and we get $\mu_{\rm eff} \sim 0.43\mu_{\rm B}$ [see Fig. 4(d)] [66]. Moreover, the crossings of different specific heat curves measured in different magnetic fields are also well captured by this U(1) Dirac scenario [Fig. 4(d)]. The real material of YCOB with bond randomness should have a distribution of hopping strength on the kagome lattice [see Fig. 5(a)], which might slightly renormalize the band structure and the dispersion around the Dirac nodes and account for the observation of $\alpha = 2.31(1) \neq 2$.

In the neighborhood of the U(1) Dirac state, the $\mathbb{Z}_2[0, \pi]\beta$ QSL was proposed as the GS of the KHA as well [16,17,63]. Therefore, we also fit the specific heat of YCOB by using the mean-field ansatz of the $\mathbb{Z}_2[0, \pi]\beta$ state [63], and obtain a similar band structure with a small zero-field spin (triplet) gap of $\sim 0.025J_1$ [see Fig. 4(f)] that is smaller than the DMRG value $\sim 0.05J_1$ [16]. The applied magnetic field tends to close the gap, form Fermi pockets, and thus increase the low-T specific heat [see Fig. 4(d)]. Similarly, by fitting we obtain the reduced $\mu_{\rm eff} \sim 0.48\mu_{\rm B}$. Finally, it is worth noting that the spin gap should be slightly overestimated because the calculated data drops faster than the experimental one at $\sim$0.4 K as $T \to 0$ K at 0 T [see Fig. 4(d)].

C. Discussion

In the sibling $YCu_3(OH)_6Cl_3$, no obvious antisite mixing of OH/Cl has been reported, the center of inversion is located at 1b, Y^{3+} almost fully occupies its ideal position, i.e., $f_{Y1} \sim 1$ [67], and a long-range magnetic transition occurs at $T_N = 12$ K $\sim 0.15J_1$ [68–70], possibly due to the DM interaction [47]. In contrast, a gapless QSL behavior is observed in YCOB (similar to Ref. [41]) with profound antisite mixing and thus bond randomness. Therefore, we believe that the bond randomness

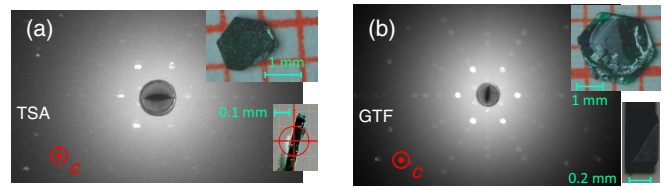

FIG. 6. Laue XRD patterns on the *ab* plane of (a) the largest TSA (the upper inset) and (b) typical GTF (the upper inset) crystals. The thicknesses of typical TSA and GTF crystals are shown in the lower insets of (a) and (b), respectively

is a critical ingredient for stabilizing the quantum paramagnetic state. Both the susceptibility and specific heat of model No. 2 indeed exhibit no sign of magnetic transition [see Figs. 3 and 4(b)], and a randomness-relevant gapless QSL state has been theoretically proposed in KHAs with a broad range of bond randomness [54]. Since QSLs are typically fragile in the ideal cases [12,15], the bond randomness caused by site mixing may make the gapless QSL behavior more robust against various inevitable perturbations in real materials, e.g., $ZnCu_3(OH)_6Cl_2$ and $YbMgGaO_4$ [71,72]. Our paper shows that YCOB is a rare KHA where the bond randomness and its influence to the QSL behavior might be precisely modeled.

Alternatively, the bond randomness may give rise to a non-QSL GS, e.g., the product state of randomly quenched spin singlets [6]. Whether the interaction randomness is fatal or vital to the QSL state in real materials is a hotly debated nontrivial issue [7]. Further dynamic studies, e.g., the spin-lattice relaxation rates, may be helpful to solve this issue, but are beyond the scope of the present paper.

IV. CONCLUSIONS AND OUTLOOK

We have characterized the magnetic properties of large YCOB single crystals. The exchange Hamiltonian is refined by magnetic susceptibilities on the orientated single crystals. We find the bond randomness is significant and plays an important role in the QSL behavior. No conventional magnetic transition is found and the specific heat exhibits a nearly quadratic temperature dependence below 1 K $\sim 0.02J_1$, which are phenomenologically consistent with the predictions of a gapless U(1) Dirac QSL or a $\mathbb{Z}_2$ QSL with a gap less than $0.025J_1$.

The exact GS nature of YCOB might be further identified by the Knight shift in nuclear magnetic resonance and by measuring inelastic neutron scattering and muon spin relaxation spectra. Future investigations of spin dynamics and correlations of YCOB are warranted and made possible through the availability of high-quality single crystals.

ACKNOWLEDGMENTS

We thank Tao Xiang, X. Hong, and C. Hess for helpful discussions and J. Schnack for providing their FLD data. The authors were supported by the National Key Research and Development Project of China, Grant No. 2017YFA0302901, the Youth Innovation Promotion Association CAS, Grant No. 2021004, and the Strategic Priority Research Program of Chinese Academy of Sciences, Grant No. XDB33000000. This paper was supported by the Fundamental Research Funds for the Central Universities, HUST: 2020kfyXJJS054.

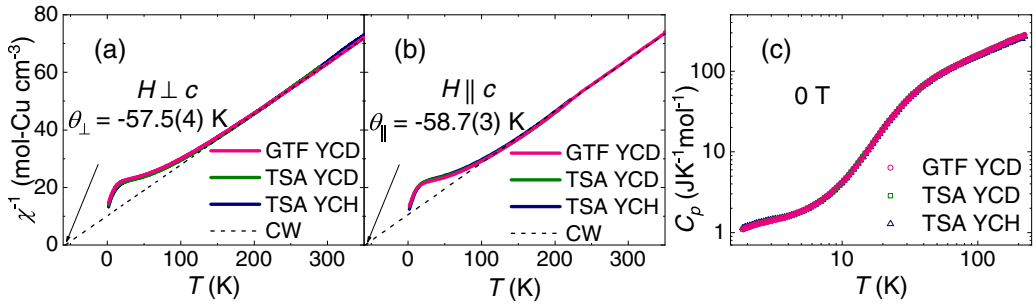

FIG. 7. Inverse dc susceptibilities (H/M) of aligned GTF single crystals of YCD (total mass 21.8 mg) measured at 1 T applied perpendicular (a) and parallel (b) to the c axis, with those of TSA crystals of YCD (net weight: 23.0 mg) and YCH (net weight: 23.8 mg) for comparison. The dashed lines present the linear (Curie-Weiss) fits to the GTF data above 150 K. (c) Specific heat of a GTF single crystal of YCD (mass 5.90 mg) measured at 0 T, with those of TSA crystals of YCD (net weight: 1.90 mg) and YCH (net weight: 1.82 mg) for comparison. No substantial sample dependence of the thermodynamic properties was observed.

APPENDIX A: SINGLE CRYSTAL GROWTH, STRUCTURAL, THERMODYNAMIC, AND ELECTRON SPIN RESONANCE CHARACTERIZATIONS

We grew single crystals of $YCu_3(OH)_{6.5}Br_{2.5}$ (YCH) and $YCu_3(OD_{0.6}H_{0.4})_{6.5}Br_{2.5}$ (YCD) in two ways. First, we synthesized the crystals in a Teflon-lined stainless steel autoclave (TSA) using the hydrothermal technique [40] reported by Chen *et al.* The high-purity D_2O ($\geqslant$99.9%, Shanghai Titan Scientific Co., Ltd) was used instead of H_2O when we synthesized YCD. Crystals with a maximum size of 1.2 × 1.2 × 0.15 mm (mass ∼0.9 mg) were obtained, as shown in Fig. 6(a).

To improve the quality and size of the single crystals, we performed a recrystallization process in a two-zone gradient tube furnace (GTF) with a temperature gradient of ∼2 °C/cm. The starting materials of $Cu(NO_3)_2 \cdot 3H_2O$ (2.416 g, 10 mmol), $Y(NO_3)_3 \cdot 6H_2O$ (7.662 g, 20 mmol), KBr (7.140 g, 60 mmol), and 4 mL D_2O were mixed together and charged into a fused quartz tube (inside diameter 14 mm, outside diameter 20 mm, a length of ∼30 cm). The tube was sealed, mounted vertically, and then heated to 230 °C in a box furnace. The temperature was maintained for three days and then decreased to room temperatures. The prereacted tube was mounted horizontally into the two-zone gradient furnace. Both the hot and cold ends were simultaneously heated to 225 and 165 °C, respectively, for 6 h. The furnace and all growth parameters were left undisturbed for 30 days, and then both ends were simultaneously cooled down to room temperatures. Transparent green single crystals with shining surfaces and a typical size of 3.1 × 2.4 × 0.25 mm (mass ∼7.4 mg) were obtained [see Fig. 6(b)]. Back-scattering Laue XRD measurements (LAUESYS_V_674, Photonic Science & Engineering Ltd) were carried out for both TSA and GTF single crystals. The GTF crystals show obviously sharper Laue photographs [please compare Fig. 6(b) to Fig. 6(a)], implying that the quality of the single crystals has been considerably improved by the above recrystallization process.

The crystal structure was obtained from the refinements of the XRD (Mo K_α, λ = 0.71073 Å, XtaLAB mini II, Rigaku Corporation) data measured on selected YCH and YCD crystals with proper sizes. We started with the crystal structure previously reported in Ref. [40] and got a very similar refined structure (see Table I). From the refinements, we find that YCH(D) has a structural composition $YCu_3[OH(D)]_6Br_2[OH(D)]_{1-x'}Br_{x'}$ with $x' = 0.43$–0.47. In comparison, a slightly larger value $x' = 0.51$ had been reported in Ref. [40]. Henceforth, we use the approximate composition $YCu_3[OH(D)]_{6.5}Br_{2.5}$ throughout this paper.

The dc magnetization and ac susceptibilities ($1.8 \leqslant T \leqslant 350$ K and $0 \leqslant \mu_0 H \leqslant 7$ T) were measured by a magnetic property measurement system (MPMS, Quantum Design) us-

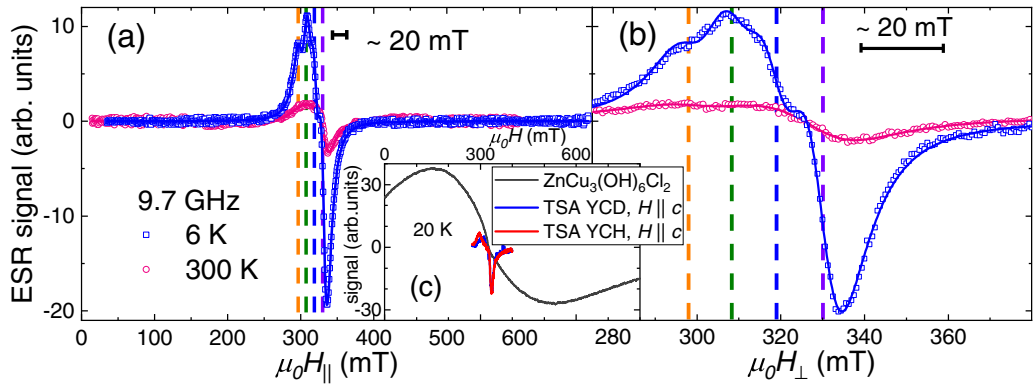

FIG. 8. The ESR spectra measured parallel (a) and perpendicular (b) to the c axis. The solid lines show the four-Lorentzian fits [see Eq. (A2)] and the dashed lines present the calculated ESR fields (see Fig. 9). (c) The x-band ESR spectra measured at 20 K on single-crystal samples of TSA YCH (23.8 mg) and YCD (23.0 mg), with the spectrum of the $ZnCu_3(OH)_6Cl_2$ powder (∼20 mg) for comparison.

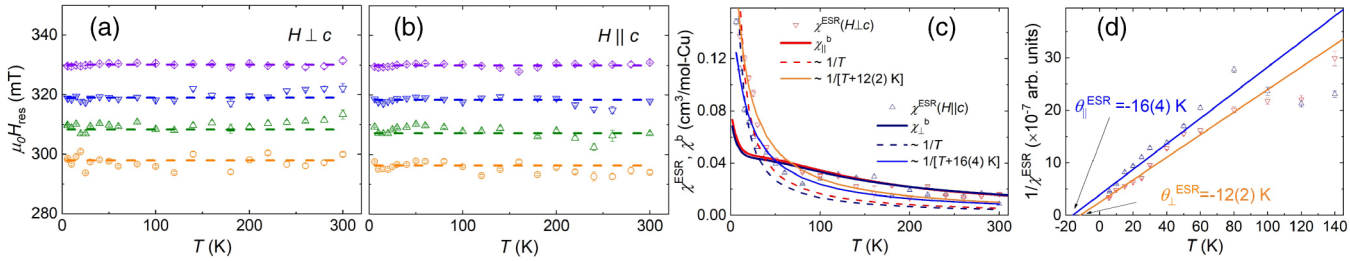

FIG. 9. ESR fields obtained from fitting the ESR spectra measured along the *ab* plane (a) and *c* axis (b), respectively (see Fig. 8). The dashed lines show the combined fit. (c) Scaling of the ESR intensities, $\chi^{\rm ESR}(H \perp c)$ and $\chi^{\rm ESR}(H \parallel c)$, with the bulk susceptibilities (thick lines), $\chi^{\rm b}_{\parallel}$ and $\chi^{\rm b}_{\perp}$, respectively. The thin dashed and solid lines present the Curie-Weiss fits with zero (i.e., Curie tails) and adjustable Curie-Weiss temperatures, respectively. (d) Inverse (integrated) ESR intensities.

ing well-aligned (by Laue XRD) single-crystal samples of ∼23 mg, whereas the magnetization up to 14 T was measured by a vibrating sample magnetometer in a physical property measurement system (PPMS, Quantum Design). At high temperatures, the magnetization of the compound is weak, and we carefully chose a quartz holder without evident background. As shown in Figs. 7(a) and 7(b), our susceptibilities follow the Curie-Weiss law between ∼120 and 350 K (the maximum measured temperature), with Curie-Weiss temperatures $\theta_{\perp} = -57.5(4)$ K and $\theta_{\parallel} = -58.7(3)$ K along the *ab* plane and *c* axis, respectively. In comparison, Chen *et al.* reported a slightly larger magnitude of the Curie-Weiss temperature of −74 K from fitting their isotropic susceptibility measured in diamagnetic gelatine capsules below ∼280 K [40].

The specific heat ($1.8 \leqslant T \leqslant 220$ K) was measured at a magnetic field of $0 \leqslant \mu_0 H_{\parallel} \leqslant 9$ T applied along the *c* axis using the single-crystal samples in a PPMS. The specific heat measurements on a selected GTF single crystal (mass 4.00 mg) between 0.36 and 2 K were conducted in a ^{3}He refrigerator. N-grease was used to facilitate thermal contact between the crystal and the puck, and the sample coupling was better than 98%. The contributions of the grease and puck under different applied fields were measured independently and subtracted from the data.

No significant sample dependence of thermodynamic properties was observed among GTF YCD, TSA YCD, and TSA YCH single crystals (see Fig. 7). Therefore, we focused on the measurements on the highly-quality GTF YCD (mentioned as YCOB) single crystals below and also throughout the main text.

The YCOB crystals are good insulators and have resistance larger than 20 MΩ measured parallel and perpendicular to the *c* axis at room temperatures. Above ∼120 K, the inverse susceptibilities of YCOB show a linear temperature dependence following the Curie-Weiss law along both the *ab* plane and *c* axis [see Figs. 7(a) and 7(b)]. We obtain the lengths of the magnetic moments $g_{\perp}\mu_{\rm B}\sqrt{S(S+1)} = \sqrt{3k_{\rm B}C_{\perp}/(N_{\rm A}\mu_0)} = 1.898(1)\mu_{\rm B}$ and $g_{\parallel}\mu_{\rm B}\sqrt{S(S+1)} = \sqrt{3k_{\rm B}C_{\parallel}/(N_{\rm A}\mu_0)} = 1.882(1)\mu_{\rm B}$ from the fitted Curie constants $C_{\perp} = 5.661(7)$ Kcm^3 per mol Cu and $C_{\parallel} = 5.568(4)$ Kcm^3 per mol Cu, respectively. By fixing $S = \frac{1}{2}$, we further get $g_{\perp} = 2.192(1)$ and $g_{\parallel} = 2.174(1)$. Moreover, the antiferromagnetic exchange energy can be roughly estimated as $J_1 \sim -3\theta_{\perp}/[4S(S+1)] \sim -3\theta_{\parallel}/[4S(S+1)] \sim 60$ K.

Derivative ESR absorption spectra were measured at 6–300 K on the aligned single-crystal samples of YCOB (total mass ∼22 mg) with the magnetic field applied parallel and perpendicular to the *c* axis, respectively, using continuous wave spectrometers (CIQTEK EPR200-Plus and Bruker EMXmicro-6/1) at *x*-band frequencies ($\nu \sim 9.7$ GHz) equipped with ^{4}He refrigerators. The single-crystal samples of YCOB were washed with high-purity water and ethanol repeatedly and in succession, and the absence of any obvious impurity phase was confirmed by using a microscope before the ESR measurements. The ESR spectra measured at various temperatures are so narrow that the distinctive hyperfine structure is clearly visible (see Fig. 8) [73,74]. Similar ESR lines usually appear in Cu^{2+}-based complexes with weak couplings [74]. However, in most existing strongly correlated 3*d* magnets, e.g., $ZnCu_3(OH)_6Cl_2$ [46] and α-CrOOH [75], broad single ESR lines are typically observed due to the magnetic anisotropy. As shown in Fig. 8, the ESR signals are still robust even at room temperatures, with the maximum strength of ∼1 (μV) at the microwave power of 0.2 mW, modulation amplitude of 0.4 mT, and magnification of 10. The integrated intensity of YCOB is about 1% of that of $ZnCu_3(OH)_6Cl_2$ reference powder, roughly consistent with the estimated concentration (∼0.8%) of the local moments [see Fig. 8(c)]. Moreover, the integrated ESR intensity roughly follows a Curie-Weiss behavior with the Curie-Weiss temperature of ∼−14 K instead of the bulk susceptibility [see Figs. 9(c) and 9(d)]. These observations suggest that the narrow ESR signals of YCOB should mainly originate from the nearly free local moments induced by the bond randomness on the kagome lattice (see main text). In contrast, the sibling $YCu_3(OH)_6Cl_3$ without evident bond randomness shows a very broad ESR signal with the linewidth of ∼7 T [47]. Therefore, the possible broad ESR lines from the strongly coupled ($J_1 \sim 60$ K) Cu spins of YCOB may not be well captured by our *x*-band (maximum applied field of ∼1 T) ESR spectrometers.

The single-ion hyperfine Hamiltonian of the Cu^{2+} ($S = \frac{1}{2}, I = \frac{3}{2}$) ions that is invariant under the D_{3d} point-group symmetry can be written as [73,74]

$$\mathcal{H}_{\rm hp} = -\mu_0\mu_{\rm B}\mathbf{H}\cdot\mathbf{g}\cdot\mathbf{S} + \mathbf{I}\cdot\mathbf{A}\cdot\mathbf{S}$$

$$= \begin{pmatrix}
\frac{3}{4}A_\parallel - \frac{1}{2}G_\parallel & 0 & 0 & 0 & \frac{i}{2}G_\perp & 0 & 0 & 0 \\
0 & \frac{1}{4}A_\parallel - \frac{1}{2}G_\parallel & 0 & 0 & \frac{\sqrt{3}}{2}A_\perp & \frac{i}{2}G_\perp & 0 & 0 \\
0 & 0 & -\frac{1}{4}A_\parallel - \frac{1}{2}G_\parallel & 0 & 0 & A_\perp & \frac{i}{2}G_\perp & 0 \\
0 & 0 & 0 & -\frac{3}{4}A_\parallel - \frac{1}{2}G_\parallel & 0 & 0 & \frac{\sqrt{3}}{2}A_\perp & \frac{i}{2}G_\perp \\
-\frac{i}{2}G_\perp & \frac{\sqrt{3}}{2}A_\perp & 0 & 0 & -\frac{3}{4}A_\parallel + \frac{1}{2}G_\parallel & 0 & 0 & 0 \\
0 & -\frac{i}{2}G_\perp & A_\perp & 0 & 0 & -\frac{1}{4}A_\parallel + \frac{1}{2}G_\parallel & 0 & 0 \\
0 & 0 & -\frac{i}{2}G_\perp & \frac{\sqrt{3}}{2}A_\perp & 0 & 0 & \frac{1}{4}A_\parallel + \frac{1}{2}G_\parallel & 0 \\
0 & 0 & 0 & -\frac{i}{2}G_\perp & 0 & 0 & 0 & \frac{3}{4}A_\parallel + \frac{1}{2}G_\parallel
\end{pmatrix}, \tag{A1}$$

under the subspace of $|S^z = \frac{1}{2}, I^z = \frac{3}{2}\rangle$, $|\frac{1}{2}, \frac{1}{2}\rangle$, $|\frac{1}{2}, -\frac{1}{2}\rangle$, $|\frac{1}{2}, -\frac{3}{2}\rangle$, $|-\frac{1}{2}, \frac{3}{2}\rangle$, $|-\frac{1}{2}, \frac{1}{2}\rangle$, $|-\frac{1}{2}, -\frac{1}{2}\rangle$, $|-\frac{1}{2}, -\frac{3}{2}\rangle$. Here, $\mathbf{H} = H[0\ \sin\theta\ \cos\theta]$ is the applied magnetic field, $G_\parallel = \mu_0\mu_{\rm B}Hg_\parallel\cos\theta$ and $G_\perp = \mu_0\mu_{\rm B}Hg_\perp\sin\theta$ are the Zeeman terms. The eight eigenstates of Eq. (A1) are represented as $|E_j^\eta\rangle$ ($j = 1, 2, ..., 8$) with increasing eigenenergies. Due to $A_\eta \ll \mu_0\mu_{\rm B}H_{\rm res}^\eta g_\eta$, these eigenstates give rise to four ESR modes with $E_{9-j'}^\eta - E_{j'}^\eta = h\nu$ and nonzero transition probabilities $\propto|\langle E_{9-j'}^\eta|2S^x|E_{j'}^\eta\rangle|^2 \sim 1$, where $j' = 1, 2, 3, 4$. These four ESR modes are governed by the transitions, $|\frac{1}{2}, I^z\rangle \rightarrow |-\frac{1}{2}, I^z\rangle$ ($I^z = -\frac{3}{2}, -\frac{1}{2}, \frac{1}{2}, \frac{3}{2}$), similar to other Cu^{2+}-based magnets [74]. Therefore, we fit the experimental ESR spectra (see Fig. 8) using

$$\frac{dI_{\rm abs}^\eta}{\mu_0 dH} = \frac{16I_0^\eta\Delta H_\eta}{\pi\mu_0^2}\sum_{j'=1}^{4}\frac{f_{j'}^\eta\left(H_{j'}^\eta - H\right)}{\left[4\left(H_{j'}^\eta - H\right)^2 + \Delta H_\eta^2\right]^2}, \tag{A2}$$

where $f_{j'}^\eta > 0$ is the spectrum weight of each ESR mode with $\sum_{j'=1}^4 f_{j'}^\eta \equiv 1$, $\mu_0\Delta H_\eta$ is the line width that is presumed to be independent of j' for simplicity, and I_0^η is the total integrated intensity that is proportional to the dynamical susceptibility in the direction perpendicular to the applied field, $I_0^\eta \propto \chi_\eta''(\mathbf{q} \rightarrow 0, \omega)$ [46]. The fitted ESR fields are almost temperature independent [see Figs. 9(a) and 9(b)]. From fitting the ESR fields both parallel ($\eta = \parallel$) and perpendicular ($\eta = \perp$) to the c axis, we obtain all the single-ion parameters, $g_\perp = 2.205(4)$, $g_\parallel = 2.211(4)$, $|A_\perp| = 15.8(2)$ mK, and $|A_\parallel| = 16.7(2)$ mK.

APPENDIX B: DFT + U CALCULATIONS

Although our single-crystal XRD measurements (see above), as well as the reported electron-microprobe analysis [40], show obvious site-mixing disorder of OH^- and Br^-, neither global symmetry reduction nor antisite mixing between Cu^{2+} and other nonmagnetic ions is probed in YCOB. To go beyond the average structure from single-crystal XRD and investigate the influence of this structural disorder on the magnetism, we conducted the DFT + U simulation, which had been widely used in other Cu^{2+}-based magnets, e.g., volborthite $Cu_3V_2O_7(OH)_2 \times 2H_2O$ [76], kapellasite $Cu_3Zn(OH)_6Cl_2$, and haydeeite $Cu_3Mg(OH)_6Cl_2$ [77]. Similar to $YbMgGaO_4$ [78], we constructed three OH/Br configurations to simulate the site mixing and optimized their geometry using DFT calculations (see Fig. 10). All possible NN environments of 1b position are included in the three configurations (see Fig. 10), and the further enlarging of supercells sharply increases the computational cost. All our DFT + U calculations were performed in the VASP code [43,44] with the generalized gradient approximation (GGA) [79]. The $6 \times 6 \times 6$ k-mesh was used, and residual forces were below 0.006 eV/Å in the fully optimized structures. The lattice parameters were fixed to the experimental values, $a = b = 6.6647$ Å and $c = 6.0093$ Å.

The random distribution of OH^- and Br^- takes place around the 1a positions, which are adjacent to the hexagons on the kagome lattice of magnetic Cu^{2+} ions (see Fig. 10). The polar OH^- ions easily make the local environments of 1b positions (i.e., the Y1 sites, located at the centers of the hexagons) nonsymmetric, and drive Y^{3+} away from its ideal 1b position, i.e., $|\Delta z_{\rm Y2}| > 0$. Our DFT calculation gives $|\Delta z_{\rm Y1}| = 0$ in the symmetric Br-Br [see Fig. 10(a)] stacking, and $|\Delta z_{\rm Y2}| \sim 0.6$ and 0.4 Å in the nonsymmetric OH–OH [see Fig. 10(b)] and Br–OH–Br [see Fig. 10(c)] cases, respectively, which are well consistent with the XRD results of $|\Delta z_{\rm Y1}| = 0$ and $|\Delta z_{\rm Y2}| \sim 0.7$ Å (Table I). Furthermore, we find that both ∠CuOCu and Cu–O, which are closely relevant to the exchange integrals, are sensitively dependent on the OH/Br distribution (see Table II). When the local environment of the 1b Wyckoff position gets nonsymmetric, the configuration of two alternate superexchanges along the hexagon is naturally expected, according to the structural symmetry [see Figs. 10(b) and 10(c)].

Starting with the optimized crystal structures, we further calculated the exchange couplings from the energy differences between the fully ferromagnetic state and various collinear states. The exchange integrals monotonically decrease with increasing Coulomb repulsion $U_{\rm eff}$ [47,76,77]. For YCOB, we fixed $U_{\rm eff} = 8.72$ eV in all GGA + U calculations and obtained the average $\bar{J}_1 = (2J_{1a}+J_{1b1}+J_{1b2}+J_{1c1}+J_{1c2}+J_{1c3}+J_{1c4})/8 = 65$ K (see

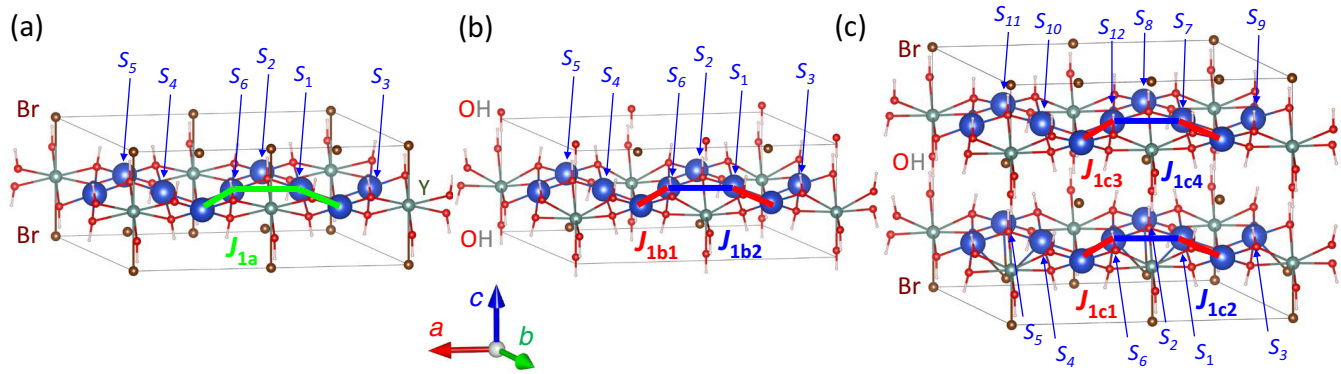

FIG. 10. Optimized crystal structures for different stacking sequences of Br/OH, (a) symmetric Br–Br [$2YCu_3(OH)_6Br_3$, supercell: $2 \times 1 \times 1$ unit cells, total energy -31.2 eV/Cu], nonsymmetric (b) OH–OH [$2YCu_3(OH)_7Br_2$, $2 \times 1 \times 1$, total energy -33.9 eV/Cu] and (c) Br–OH–Br [$4YCu_3(OH)_{6.5}Br_{2.5}$, $2 \times 1 \times 2$, total energy -32.5 eV/Cu]. The indices of Cu^{2+} (blue ball) spins and superexchanges are marked. It is worth noting that the symmetric OH-HO configuration (total energy -33.6 eV/Cu) isn't energetically favorable compared to the nonsymmetric one [see (b), total energy -33.9 eV/Cu].

Table III), in good agreement with the experimental result of $|\theta_\perp| \sim |\theta_\parallel| \sim 60$ K. From fitting these energy differences, we obtain the exchange couplings for each stacking sequence of Br/OH (see Table III).

Based on the above DFT + U calculations, the following conclusions can be drawn:

(1) In YCOB, all long-distance couplings beyond NNs are negligible, $|J_2|/\bar{J}_1 < 4\%$, $|J_3|/\bar{J}_1 < 2\%$, $|J_d|/\bar{J}_1 < 2\%$, and $|J_\perp|/\bar{J}_1 < 2\%$ (see Table III), due to the spatial localization of the $3d$ electrons (highly similar to $YCu_3(OH)_6Cl_3$ [47]). This significantly simplifies the exchange model for YCOB.

(2) The antisite disorder of OH/Br strongly influences the NN exchange couplings (J_1) and causes the alternation of two NN exchanges along the randomly distributed ($1-f_{Y1} \sim 70\%$) nonsymmetric hexagons of the kagome lattice, $(J_{1c3} - J_{1c4})/(J_{1c3} + J_{1c4})$ ~0.03, $(J_{1b1} - J_{1b2})/(J_{1b1} + J_{1b2})$ ~0.43, and $(J_{1c1} - J_{1c2})/(J_{1c1} + J_{1c2})$ ~1.26.

(3) There exist no orphan spins, even in the presence of the mixing between OH and Br. The antisite disorder occurs around the high-symmetry Wyckoff position, $1a$, and thus the weaker and stronger bonds alternate along the hexagon in the nonsymmetric environment. Although one of the alternate ∠CuOCu may be profoundly reduced to ~108.2° (see Table II), and the strength of the coupling can be surprisingly weak, e.g., $|J_{1c2}| \sim 11$ K, there exist no orphan Cu^{2+} spins that are weakly coupled to all the other ones.

Similar to the case of the nonmagnetic impurities in the KHA [55–57], nearly free local moments can nevertheless be induced by the bond randomness in YCOB, which accounts for almost all the low-temperature observations (see main text for model No. 2), including the weak upturn seen in susceptibilities, the slight polarization in magnetization, and the very narrow ESR signals (see above).

APPENDIX C: REFINEMENT OF THE EXCHANGE HAMILTONIAN

In this Appendix, we make great efforts to determine the exchange Hamiltonian of the KHA YCOB. At present, we have collected both susceptibility and specific heat data of YCOB, which can be used to refine the spin Hamiltonian. However, it is still extremely challenging to precisely extract the magnetic contribution from the total specific heat above ~10 K (see Appendix D) in the absence of nonmagnetic reference compounds. Therefore, below we mainly focus on the magnetic susceptibilities of the YCOB single crystal measured both parallel and perpendicular to the c axis.

1. No evident orphan spins

In YCOB, the significant antisite disorder between magnetic Cu^{2+} and other nonmagnetic ions, i.e., Y^{3+}, $H(D)^+$, O^{2-}, Br^-, is expected to be prohibited owing to the large differences in ionic charges and radii, and thus orphan spins should be negligible without any obvious impurity phases [40,41]. Following the method previously used in KHA herbertsmithite [22], we try to reproduce the magnetization measured at 2 K and up to 14 T ($\mu_B g_\eta \mu_0 H \sim 0.35 J_1$) parallel and perpendicular to the c axis by a combination of a Brillouin function for free spins and a linear magnetization for intrinsic

TABLE II. Optimized bond angles of ∠CuOCu and bond lengths of Cu–O for different stacking sequences, as well as the NN exchange couplings calculated by DFT + U (see Table III).

Supercells	∠CuOCu	Cu–O	Coupling	∠CuOCu	Cu–O	Coupling	∠CuOCu	Cu–O	Coupling	∠CuOCu	Cu–O	Coupling
Br–Br	115.5°	1.97 Å	$J_{1a} = 56$ K									
OH–OH	116.0°	1.97 Å	$J_{1b1} = 94$ K	112.7°	1.99 Å	$J_{1b2} = 38$ K						
Br–OH–Br	116.6°	1.99 Å	$J_{1c1} = 93$ K	108.2°	2.02 Å	$J_{1c2} = -11$ K	117.0°	1.95 Å	$J_{1c3} = 101$ K	116.8°	1.96 Å	$J_{1c4} = 95$ K

TABLE III. Collinear magnetic states and their energy differences from the fully ferromagnetic state. From fitting these energy differences, we obtain the exchange couplings, including NN J_1, second-neighbor J_2, and interlayer $J_\perp$. The least-squares standard deviation is defined as $\sigma = \sqrt{\frac{1}{N_0}\sum_i (X_i^{\rm DFT} - X_i^{\rm fit})^2}$, where $X_i^{\rm DFT}$ and $X_i^{\rm fit}$ are the DFT and fitted values, respectively, and N_0 is the number of the data points.

Br–Br, $St = \lvert S_1^z S_2^z S_3^z S_4^z S_5^z S_6^z\rangle$	$\lvert\downarrow\uparrow\uparrow\downarrow\uparrow\uparrow\rangle$	$\lvert\downarrow\downarrow\uparrow\downarrow\uparrow\uparrow\rangle$	$\lvert\downarrow\uparrow\uparrow\uparrow\uparrow\uparrow\rangle$	$\lvert\uparrow\downarrow\uparrow\downarrow\uparrow\uparrow\rangle$	$\lvert\uparrow\downarrow\downarrow\downarrow\uparrow\uparrow\rangle$	$\lvert\uparrow\downarrow\downarrow\downarrow\downarrow\uparrow\rangle$	$\lvert\uparrow\uparrow\downarrow\uparrow\uparrow\uparrow\rangle$
DFT + U, $E(\lvert\uparrow\uparrow\uparrow\uparrow\uparrow\uparrow\rangle) - E(St)$ (K)	232.7	234.4	117.7	231.4	229.3	174.4	116.9
Least-squares fitted $E(\lvert\uparrow\uparrow\uparrow\uparrow\uparrow\uparrow\rangle) - E(St)$ (K)	233.2	234.1	117.5	230.8	229.9	174.9	115.7
Exchange couplings and standard deviation	$J_{1a} = 56.2$ K, $J_{2a} = 2.0$ K, $J_{3a} = -0.4$ K, $J_{da} = 1.2$ K, and $\sigma_a = 0.6$ K						
OH–OH, $St = \lvert S_1^z S_2^z S_3^z S_4^z S_5^z S_6^z\rangle$	$\lvert\downarrow\uparrow\uparrow\downarrow\uparrow\uparrow\rangle$	$\lvert\downarrow\downarrow\uparrow\downarrow\uparrow\uparrow\rangle$	$\lvert\downarrow\uparrow\uparrow\uparrow\uparrow\uparrow\rangle$	$\lvert\uparrow\downarrow\uparrow\downarrow\uparrow\uparrow\rangle$	$\lvert\uparrow\downarrow\downarrow\downarrow\uparrow\uparrow\rangle$	$\lvert\uparrow\downarrow\downarrow\downarrow\downarrow\uparrow\rangle$	$\lvert\uparrow\uparrow\downarrow\uparrow\uparrow\uparrow\rangle$
DFT + U, $E(\lvert\uparrow\uparrow\uparrow\uparrow\uparrow\uparrow\rangle) - E(St)$ (K)	265.7	264.4	132.0	263.0	260.9	224.8	132.2
Least-squares fitted $E(\lvert\uparrow\uparrow\uparrow\uparrow\uparrow\uparrow\rangle) - E(St)$ (K)	265.9	264.7	131.7	262.5	261.3	224.8	131.7
Exchange couplings and standard deviation	$J_{1b1} = 94$ K, $J_{1b2} = 38$ K, $J_{2b} = 0.5$ K, $J_{3b} = -0.6$ K, $J_{db} = -0.6$ K, and $\sigma_b = 0.3$ K						
Br–OH–Br, $St = \lvert S_1^z S_2^z S_3^z S_4^z S_5^z S_6^z S_7^z S_8^z S_9^z S_{10}^z S_{11}^z S_{12}^z\rangle$	$\lvert\downarrow\uparrow\uparrow\downarrow\uparrow\uparrow\uparrow\uparrow\uparrow\uparrow\uparrow\uparrow\rangle$	$\lvert\uparrow\uparrow\uparrow\uparrow\uparrow\uparrow\downarrow\uparrow\uparrow\downarrow\uparrow\uparrow\rangle$	$\lvert\downarrow\uparrow\uparrow\downarrow\uparrow\uparrow\uparrow\downarrow\downarrow\uparrow\downarrow\downarrow\rangle$	$\lvert\downarrow\uparrow\uparrow\uparrow\uparrow\downarrow\uparrow\downarrow\uparrow\uparrow\downarrow\uparrow\rangle$	$\lvert\uparrow\uparrow\downarrow\downarrow\downarrow\uparrow\uparrow\uparrow\downarrow\downarrow\downarrow\uparrow\rangle$	$\lvert\uparrow\uparrow\downarrow\downarrow\downarrow\uparrow\uparrow\uparrow\uparrow\uparrow\uparrow\uparrow\rangle$	$\lvert\uparrow\uparrow\uparrow\uparrow\uparrow\uparrow\uparrow\uparrow\uparrow\downarrow\downarrow\downarrow\uparrow\rangle$
DFT + U, $E(\lvert\uparrow\uparrow\uparrow\uparrow\uparrow\uparrow\uparrow\uparrow\uparrow\uparrow\uparrow\uparrow\rangle) - E(St)$ (K)	172.7	400.4	570.3	565.1	398.6	194.6	209.5
Least-squares fitted $E(\lvert\uparrow\uparrow\uparrow\uparrow\uparrow\uparrow\uparrow\uparrow\uparrow\uparrow\uparrow\uparrow\rangle) - E(St)$ (K)	171.3	399.0	571.7	565.1	399.0	194.1	209.0
Exchange couplings and standard deviation	$J_{1c1} = 93$ K, $J_{1c2} = -11$ K, $J_{1c3} = 101$ K, $J_{1c4} = 95$ K, $J_{2c} = 1.3$ K, $J_{\perp c} = 0.7$ K, and $\sigma_c = 0.9$ K						

kagome spins [see Fig. 2(a)],

$$M_\eta = \frac{f_\eta g_\eta N_{\rm A}\mu_{\rm B}}{2}\frac{\exp\left(\frac{\mu_{\rm B} g_\eta \mu_0 H}{k_{\rm B}T}\right) - 1}{\exp\left(\frac{\mu_{\rm B} g_\eta \mu_0 H}{k_{\rm B}T}\right) + 1} + \chi_i^\eta H, \tag{C1}$$

where f_η and χ_i^η are fitting parameters for the fraction of free spins and nonsaturated intrinsic susceptibilities, respectively. We obtain $f_\parallel = 0.80\%$, $\chi_i^\parallel = 0.048$ cm^3/mol-Cu and $f_\perp = 0.75\%$, $\chi_i^\perp = 0.043$ cm^3/mol-Cu parallel and perpendicular to the c axis, respectively.

However, when the formalism of the free spins is extended to the specific heat, we find an obvious inconsistency. The specific heat contributed by free spins is given by

$$C_f(\mu_0 H_\parallel) = f_\parallel R\frac{\left[\frac{\Delta E(\mu_0 H_\parallel)}{k_{\rm B}T}\right]^2 \exp\left[\frac{\Delta E(\mu_0 H_\parallel)}{k_{\rm B}T}\right]}{\left\{\exp\left[\frac{\Delta E(\mu_0 H_\parallel)}{k_{\rm B}T}\right] + 1\right\}^2}, \tag{C2}$$

where $\Delta E(\mu_0 H_\parallel) = \mu_{\rm B} g_\eta \mu_0 H_\parallel$ is the energy gap between two Zeeman levels of free spins under the magnetic field of $H_\parallel$ applied along the c axis. At 2 T, the calculated C_f/T displays an obvious peak at $T = 0.9$ K [see the green line in Fig. 2(b)], while the total measured one ($C_{\rm p}/T$) shows no sign of peaks below 1.5 K. Moreover, at 0.36 K the Schottky specific heat $C_f/T = 0.067$ JK^{-2}/mol-Cu calculated at 0.4 T is even larger than the total ones, 0.038 and 0.043 JK^{-2}/mol-Cu measured at 0 and 2 T, respectively [Fig. 2(b)]. In the model widely used in other frustrated magnets, e.g., $ZnCu_3(OH)_6Cl_2$ [23] and $[NH_4]_2[C_7H_{14}N][V_7O_6F_{18}]$ [34], both the lattice and intrinsic magnetic specific heat is believed to be independent of applied magnetic field up to ~9 T, and thus their contributions are expected to be completely canceled out in the subtracted data, $\Delta C_{\rm p}/T = [C_{\rm p}(0\ {\rm T}) - C_{\rm p}(\mu_0 H_\parallel)]/T$, as shown in Fig. 2(c). However, the Schottky model $[C_f(0\ {\rm T}) - C_f(\mu_0 H_\parallel)]/T$, see Eq. (C2) for C_f] with $f_\parallel = 0.80\%$ clearly fails to capture the subtracted data of YCOB, with a rather large residual $R_p = 32.3 \gg 1$ [see Eq. (1) for the definition of R_p]. Following Refs. [23,34], we also treat both $f_\parallel$ and $\Delta E(\mu_0 H_\parallel)$ as adjustable parameters, and obtain $f_\parallel = 0.04$, $\Delta E(0\ {\rm T}) = 7.4$ K, $\Delta E(2\ {\rm T}) = 7.7$ K, $\Delta E(6\ {\rm T}) = 9.5$ K, and $\Delta E(9\ {\rm T}) = 11.4$ K with the least $R_p = 17.4 \gg 1$. In sharp contrast to $ZnCu_3(OH)_6Cl_2$ [23], $[NH_4]_2[C_7H_{14}N][V_7O_6F_{18}]$ [34], and $ZnCu_3(OH)_6SO_4$ [36], etc., the fitted $\Delta E(\mu_0 H_\parallel)$ in YCOB clearly deviates far from the expected Zeeman energy gap of free spins.

The above inconsistency unambiguously demonstrates that the concentration of orphan spins is much lower than 0.8%. The slight polarization and weak upturn observed in the low-T (below $0.2J_1$) magnetization and susceptibilities, respectively, should be governed by the intrinsic magnetic properties of the KHA YCOB. Based on the DFT + U calculations discussed in Appendix B, the site mixing between OH and Br causes two alternate exchanges along 70% of the hexagons on the kagome lattice and leads to the random model No. 2, which resolves the above inconsistency naturally [see main text for the reproduction of the weak upturn and slight polarization, and see Fig. 2(c) for the simulations of the specific heat differences above ~7 K ~$0.1J_1$].

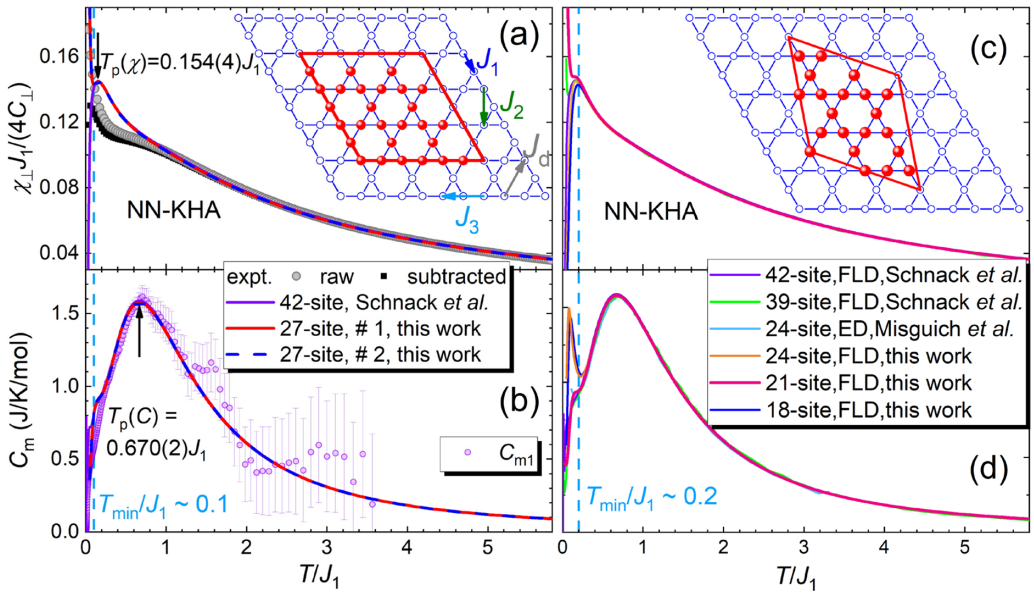

FIG. 11. Calculated magnetic susceptibility (a) and specific heat (b) of the 27-site NN-KHA cluster as function of normalized temperature (T/J_1) at zero field, with the reported 42-site FLD results [50] for comparison. The size effect is negligible at $T \geqslant 0.1J_1$. The inset of (a) shows the 27-site KHA cluster with the Heisenberg exchange interactions (colored arrows). Calculated magnetic susceptibility (c) and specific heat (d) of the 24-, 21-, and 18-site NN-KHA clusters as function of normalized temperature at zero field, with the reported 24-site ED [81], 39-, and 42-site FLD [50] results for comparison. The inset of (c) displays the 21-site KHA cluster. The size effect of susceptibility is negligible at $T \geqslant 0.2J_1$, whereas the specific heat shows size effect below $\sim 0.3J_1$.

Even when the Brillouin function for 0.8% of the free spins is subtracted from the raw susceptibilities [see Fig. 2(d)], we find that the final refinement results keep almost unchanged [80], as the difference is really trivial above $T_{\rm min} = 6$ K (see Fig. 13). Therefore, we use the experimental raw susceptibilities to refine the exchange Hamiltonian below.

2. Finite-temperature Lanczos diagonalization method

We carried out FLD calculations for the thermodynamic properties on 18-, 21-, 24-, and 27-site kagome clusters with PBCs [75,82] [insets of Figs. 11(a) and 11(c)]. Forty Lanczos steps and ten different randomly chosen states were used in all our FLD calculations. The finite-size effect of susceptibility turns out to be negligible above $T_{\rm min} = 0.1J_1 \sim 7$ K and $0.2J_1 \sim 12$ K for the 27- and 21- (18-, 24-) site FLD calculations, respectively, with the error less than $\sim$1% compared to the reported 42-site results [50] (see Fig. 11). In our 27-site FLD calculations, $S^z \equiv \sum_j S_j^z$ symmetry of the system was used, and the exact diagonalization calculations were conduced in the subspaces of $|S^z| \geqslant 23/2$ [50]. No obvious difference between two independent 27-site FLD calculations is found [see Figs. 11(a) and 11(b)]. In the ideal $S = \frac{1}{2}$ NN-KHA case, broad peaks of our calculated magnetic susceptibility and specific heat appear at $T_{\mathbf{p}}(\chi) = 0.154(4)J_1$ and $T_{\mathbf{p}}(C) = 0.670(2)J_1$, respectively, which are well consistent with previously reported results [50].

The ideal $S = \frac{1}{2}$ NN-KHA model can't precisely capture the magnetic susceptibilities measured on YCOB below $T \sim 0.6J_1 \sim 40$ K [see Fig. 11(a)]. To better understand the thermodynamic observations, we consider a more complicated spin Hamiltonian with bond randomness. In this section, we first fixed the NN exchange coupling at $J_1 = 1$ and calculated the thermodynamic quantities with varying strength of the perturbations. Thereupon, we simultaneously fit the magnetic susceptibilities of YCOB measured both parallel and perpendicular to the c axis above $T_{\rm min}$ through fine-tuning J_1 and g by minimizing the following loss function [see Eq. (1)].

3. Bond randomness

Based on the crystal structure determined by XRD (see Table I) as well as our DFT + U calculations (see Appendix B), we constructed model No. 2 with randomly distributed hexagons of alternate bonds (see main text) and performed FLD calculations on the 18-, 21-, 24-, and 27-site clusters with PBCs. The calculated thermodynamic data are evaluated over 80, 80, 40, and 36 independent samples for the 18-, 21-, 24-, and 27-site FLD calculations, respectively, that have led to fully converged results of the random KHA ($X_i^{\rm cal}$) (see Fig. 12). The fluctuation of the bonds ($\Delta J/J_1$) gradually induces local moments, which account for the growth of the upturn in susceptibility and the decrease of the finite-size effect of the FLD calculations. At $\Delta J/J_1 \geqslant 0.7$, the finite-size effect almost disappears and our FLD simulations get very convincing even at low temperatures ($T \sim 0.1J_1$). Both the weak upturn below $\sim 0.5J_1$ and broad hump at $\sim J_1$ seen in susceptibilities can be excellently reproduced by this model (see Fig. 12).

If the local symmetries of the bond randomness aren't taken into account and conventional Lorentzian distributions of the exchange couplings and g factors are introduced (the average values are $\langle J_1 \rangle$ and $\langle g \rangle$, and the full widths at half maximum are ΔJ_1 and Δg) [8,52,53,78,83,84], there's no way one can better fit the magnetic susceptibilities measured on YCOB, and the residual R_p increases monotonically with the

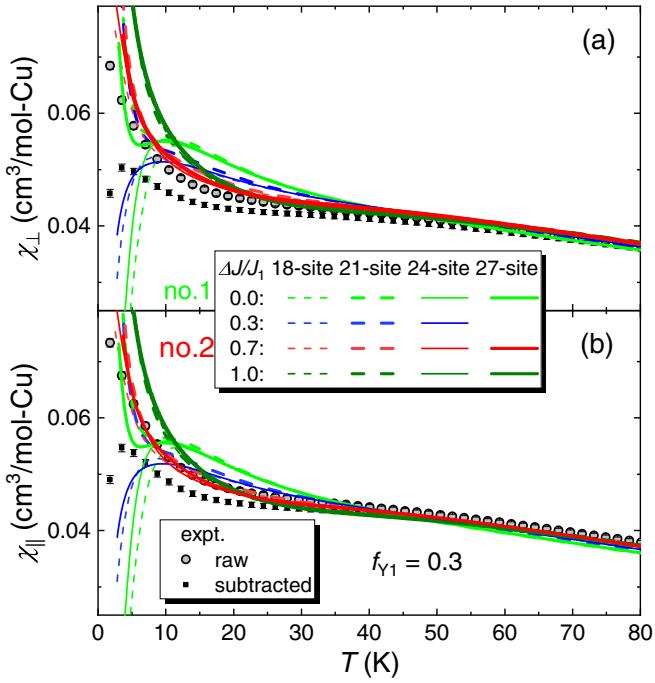

FIG. 12. (a), (b) Least-R_p fits to the experimental raw susceptibilities with different fixed fluctuations of exchange couplings, $\Delta J/J_1$, at $f_{Y1} = 0.3$ experimentally determined by XRD, above 6 K. The FLD calculations on various size random KHA clusters are conducted, and the finite-size effect is almost negligible at $\Delta J/J_1 \geqslant 0.7$ [see (a) and (b)]. For clarity, we present here only the low-T data, please see main text for the full temperature range.

complete and continuous randomness (see Fig. 13) because the complete and continuous randomness fails to reproduce the characteristic hump seen in susceptibilities at $\sim J_1$. The above analysis further validates our microscopic exchange model No. 2 based on the crystal structure and DFT + U calculations for YCOB.

APPENDIX D: MAGNETIC SPECIFIC HEAT AND ENTROPY

Above ~10 K, extracting precise magnetic specific heat from the total measured one is an extremely challenging task in the absence of nonmagnetic reference compounds. Recently, a relatively convincing method had been reported in frustrated magnets $YCu_3(OH)_6Cl_3$ [47] and α-CrOOH(D) [75]. In this method, one first fits the total measured specific heat by using a combination of a typical Debye-Einstein lattice model and the fixed FLD result (the spin Hamiltonian determined by magnetization/susceptibility measurements is fixed) well above $T_{\min}$. After subtracting the refined Debye-Einstein lattice contribution, one obtains the magnetic specific heat in the full temperature range.

In the case of YCOB, we use the 27-site FLD specific heat results calculated from the pure NN-KHA ($C_{\rm NN}$, $J_1 =$ 61.9 K, model No. 1) and random Hamiltonians ($C_{\rm ra}$, $J_1 =$ 50 K and $\Delta J = 0.7J_1$, model No. 2), and choose to fit the total measured specific heat above 30 K through tuning the Debye and Einstein temperatures [see Figs. 14(a) and 14(b)]. Each unit cell of YCOB has ~19.5 atoms (see Table I), and thus three acoustic and ~55.5 optical vibration modes. Therefore, we use a similar Debye-Einstein function previously reported

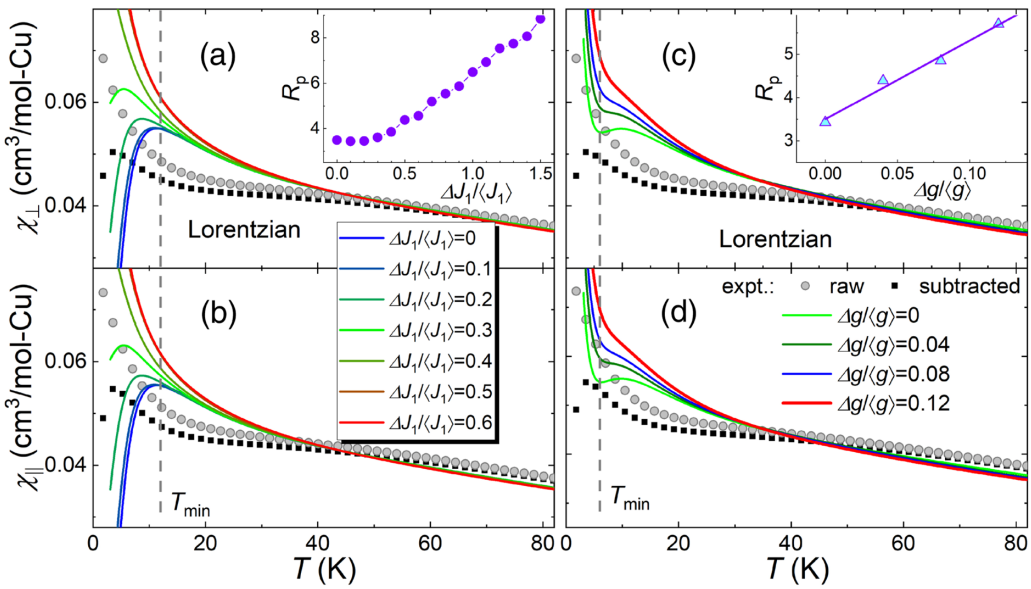

FIG. 13. (a), (b) Calculated susceptibilities of 18-site NN-KHA clusters with the Lorentzian distribution of the NN Heisenberg interactions. (c), (d) Calculated susceptibilities of 27-site NN-KHA clusters with Lorentzian distribution of the g factors. The experimental raw data of YCOB measured perpendicular and parallel to the c axis are shown by gray circles, the data subtracted by the Brillouin functions for ~0.8% of free spins are displayed by black squares, and the dashed lines mark the lower valid bounds of the 18- and 27-site FLD simulations $T_{\min} = 0.2J_1$ and $0.1J_1$, respectively, in the ideal KHA case. The insets of (a) and (c) display the randomness strength dependence of the deviation R_p (fit to data above $T_{\min}$).

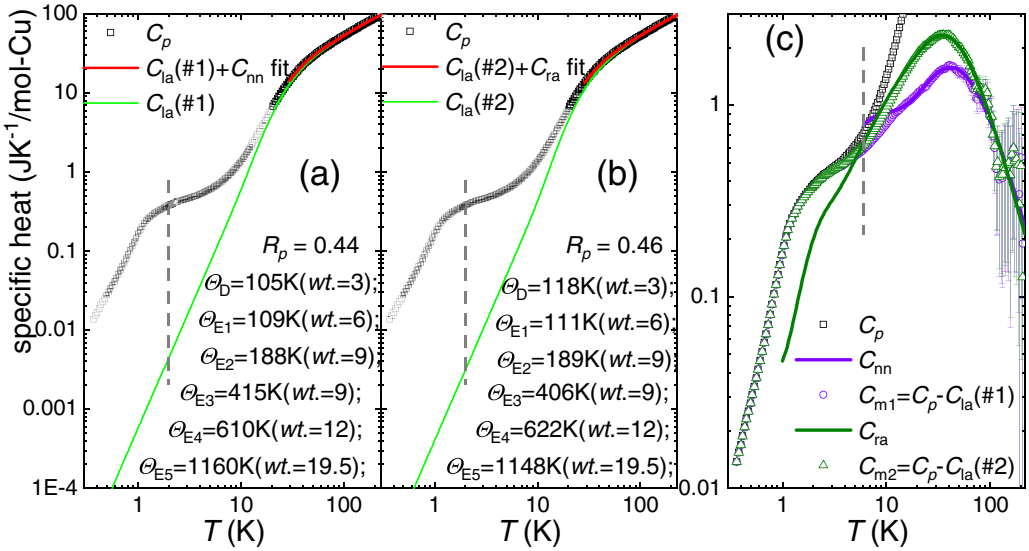

FIG. 14. (a), (b) Temperature dependence of the total specific heat (C_p, per mol Cu^{2+}) measured on the YCOB single crystal at 0 T. The red lines show the least-R_p fit using fixed models No. 1 (pure NN-KHA, see a) and No. 2 [with randomly distributed hexagons of alternate bonds, see (b)] and the green lines present the resulting lattice contributions (C_{la}). (c) Magnetic specific heat of YCOB, with C_p for comparison. The violet and olive lines display the specific heat calculated by using models No. 1 (C_{NN}) and No. 2 (C_{ra}), respectively.

in Ref. [75] for YCOB,

$$3C_{la} = \frac{9RT^3}{\Theta_D^3}\int_0^{\frac{\Theta_D}{T}} \frac{\xi^4 e^{\xi}}{(e^{\xi}-1)^2} d\xi + \frac{R}{T^2}\sum_{n=1}^{5} \frac{w_n \Theta_{En}^2 e^{\frac{\Theta_{En}}{T}}}{(e^{\frac{\Theta_{En}}{T}}-1)^2}, \tag{D1}$$

where Θ_D and Θ_{En} are fitting parameters. From fitting, we obtain two series of very similar Debye and Einstein temperatures [Θ_D and Θ_{En} ($n = 1, 2, 3, 4, 5$), listed in Figs. 14(a) and 14(b)] by fixing $w_1, w_2, w_3, w_4, w_5 = 6, 9, 9, 12, 19.5$, respectively. We further calculate (extrapolate) the Debye-Einstein lattice specific heat using Eq. (D1) in the full temperature range [see Figs. 14(a) and 14(b)] and get the magnetic specific heat by removing the lattice contributions [47]. As shown in Fig. 14(c), the resulting magnetic specific heat, C_{m1} and C_{m2}, indeed show little dependence upon the starting KHA model below ~6 K. To be completely unbiased, we never use the specific heat data above 2 K to refine the spin Hamiltonian throughout this paper.

There is no difference between C_{m1} and C_{m2} below ~6 K, and thus we only show C_{m1} in Figs. 15(b) and 15(c). Below 2 K, the lattice specific heat is completely negligible, which is more than two orders of magnitude smaller than the total C_p measured on YCOB [see Figs. 14(a) and 14(b)]. The (magnetic) specific heat of YCOB shows a power-law behavior, $C_m \propto T^{\alpha}$ at $T < 1$ K [see Fig. 15(b)]. Alternatively, one could fit the low-temperature specific heat assuming an exponential behavior, $C_m \propto \exp(-\Delta_g/T)$, but such a fit extends only up to 0.4 K with a very small gap $\Delta_g \leqslant 0.9$ K $= 0.015J_1$ [see Fig. 15(c)]. Below ~1 K, the temperature dependence of magnetic entropy flattens out at $S_m \leqslant 1.3\%R \ln 2$ [see Fig. 15(d)], suggesting that we are indeed accessing the GS properties. The final increase of the magnetic entropy of using model No. 2 from 0.36 to 220 K is closer to the expected value of $R \ln 2$ based on the third law of thermodynamics than those of using other models, possibly further confirming the validation of the random model No. 2 in YCOB.

APPENDIX E: SCALING PLOT OF SPECIFIC HEAT.

Recently, Kimchi *et al.* developed a theory for the scaling collapse based on an emergent random-singlet regime in frustrated disordered quantum spin systems [60]. This theory is applicable to lots of spin-$\frac{1}{2}$ quantum magnets including $LiZn_2Mo_3O_8$ and $ZnCu_3(OH)_6Cl_2$, where the low-T specific heat behaves as $C(H,T)/T \sim H^{-\gamma}F_q(T/H)$. Here, F_q is a general scaling function [60].

Above ~$0.02J_1$ ~ 1.2 K, the temperature and field dependence of the magnetic heat capacity of YCOB are highly similar to those of $LiZn_2Mo_3O_8$ (see Fig. 16) [60] and indeed show a scaling collapse with a familiar $\gamma \sim 0.33$–0.47 (see Fig. 16) owing to the bond randomness. However, below ~$0.02J_1$ ~ 1.2 K, the zero-field magnetic specific heat of YCOB C_m/T increases with temperature, $C_m/T \sim T^{1.31(1)}$ [see Fig. 15(b)], giving rise to a negative $\gamma = -1.31(1)$. However, the theory for the scaling collapse is based on the nonuniversal exponent $0 \leqslant \gamma \leqslant 1$ and thus obviously isn't applicable to YCOB below the crossover temperature of ~$0.02J_1$ ~ 1.2 K [see Figs. 16(b) and 16(d)].

APPENDIX F: MEAN-FIELD ANSATZ OF VARIOUS SPIN-LIQUID STATES.

In this Appendix, we try to understand the specific heat behavior of YCOB below ~2 K, where the lattice contribution is completely negligible and the raw measured data directly reflect the GS properties of the spin system. Since no conventional magnetic transition is found in YCOB, we start with the effective mean-field models (i.e., mean-field ansatz) of various QSLs, including the uniform RVB, U(1) Dirac, and $\mathbb{Z}_2$ states on the kagome lattice.

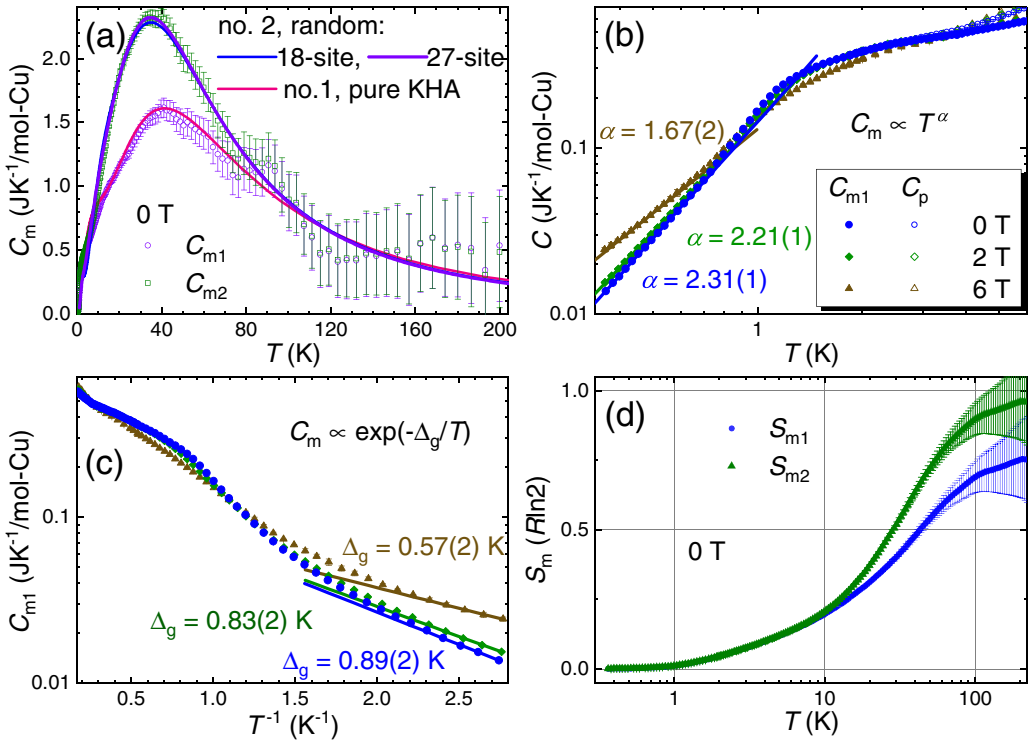

FIG. 15. (a) Magnetic specific heat of YCOB (C_{m1} and C_{m2}) obtained by subtracting the refined lattice contributions from the total one (see Fig. 14). The colored lines represent the specific heat calculated by using models No. 1 and No. 2 (see main text). (b) The magnetic specific heat of YCOB (C_{m1}) with colored lines showing the power-law fits. The raw C_p data are shown for comparison. (c) The corresponding C_{m1} versus T^{-1} plot with colored lines showing the exponential fits below 0.4 K. (d) Magnetic entropy of YCOB, S_{m1} and S_{m2}, obtained from integrating C_{m1}/T and C_{m2}/T, respectively.

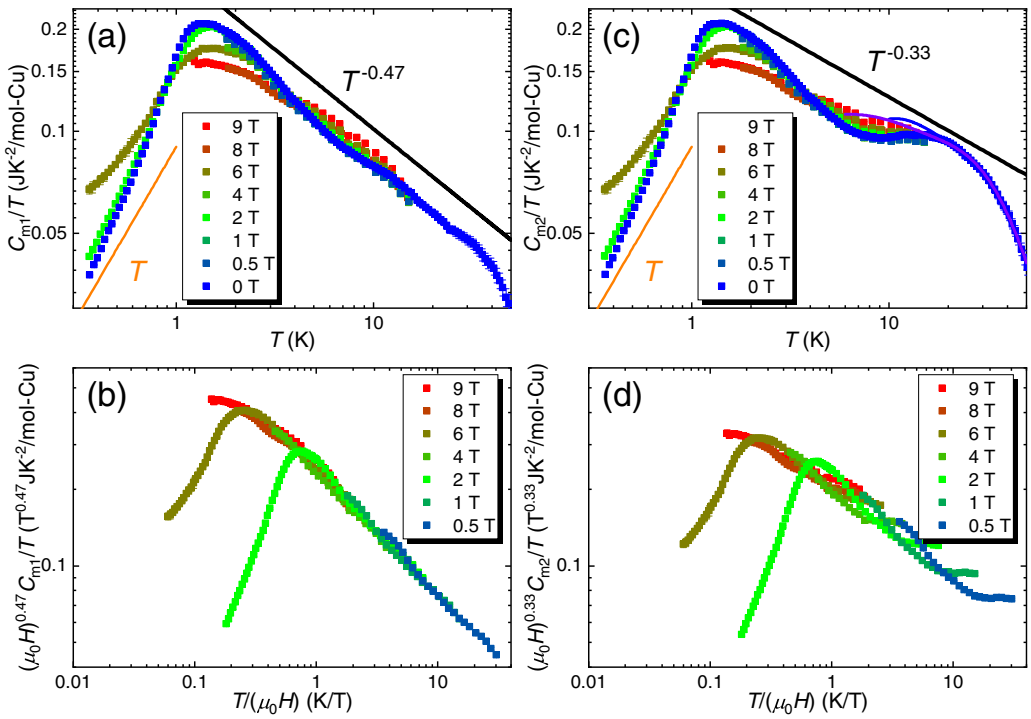

FIG. 16. (a), (c) Temperature dependence of magnetic specific heat C_{m1} and C_{m2} under various magnetic fields applied along the c axis. Above ∼1.2 K, the zero-field data roughly show power-law behaviors, $C_{m1}/T \sim T^{-0.47}$ (a) and $C_{m2}/T \sim T^{-0.33}$ (c), respectively. The orange lines mark the quadratic behavior $C_m/T \propto T$. (b), (d) Data collapse in YCOB observed above ∼1.2 K.

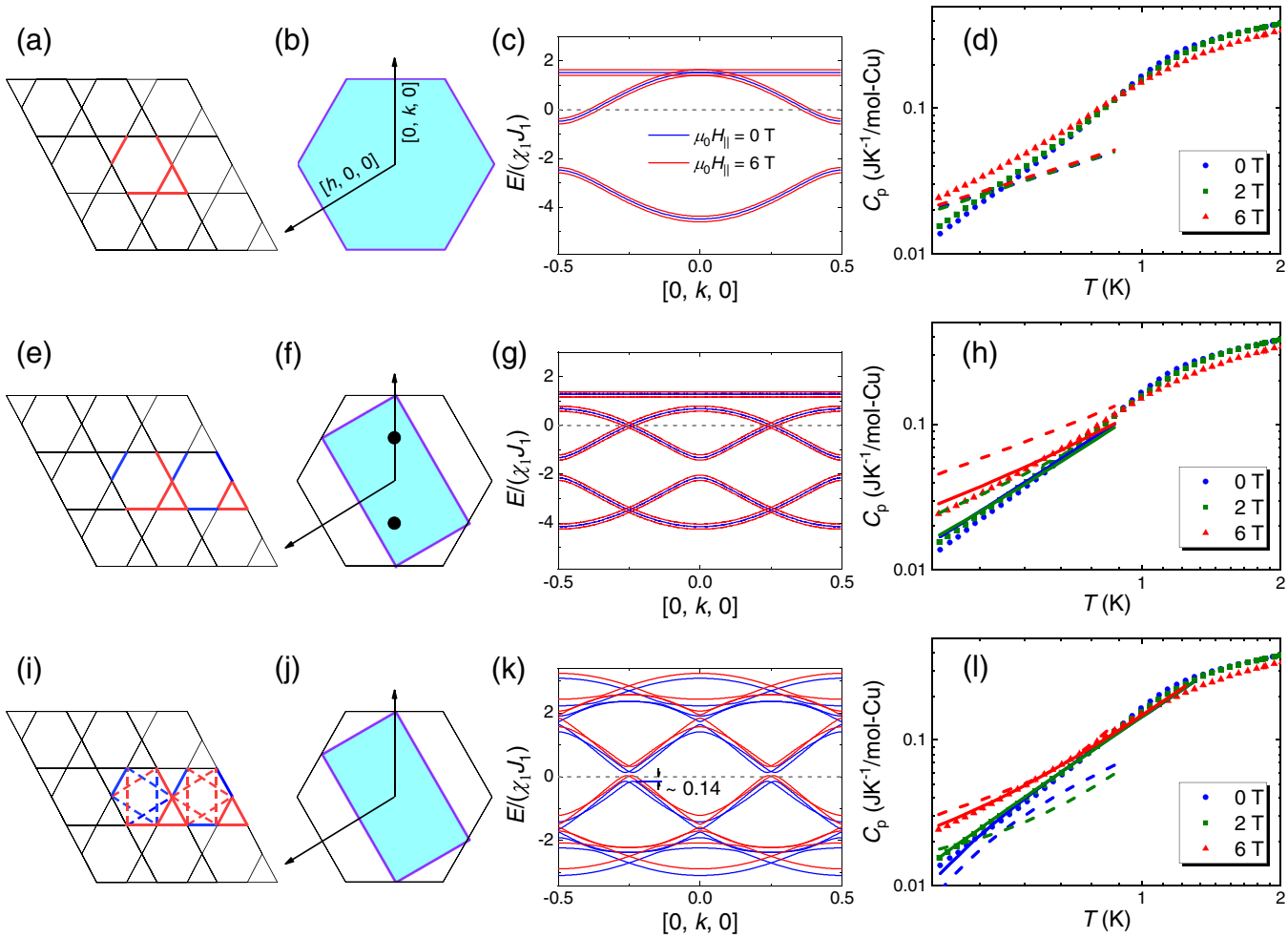

FIG. 17. (a), (e), (i) Kagome lattice showing the sign structures of hopping terms in a unit cell. Red and blue solid lines present the first neighbors $v_{jl} = 1$ and -1, whereas the red and blue dashed lines (i) present the second neighbors $v_{jl'} = 1$ and -1, respectively. (b), (f), (j) The first Brillouin zone for the uniform RVB, U(1) Dirac, and $\mathbb{Z}_2[0, \pi]\beta$ QSL states. The outer hexagons show the first Brillouin zone for the kagome lattice with the arrows showing the $[h, 0, 0]$ and $[0, k, 0]$ directions. The black circles mark the positions of the Dirac nodes in (f). (c), (g), (k) The band structures of the uniform RVB, U(1) Dirac, and $\mathbb{Z}_2[0, \pi]\beta$ QSL states along the $[0, k, 0]$ direction at $h = 0$. The calculated band structures in 0 and 6 T are shown by the blue and red lines, respectively. In the cases of (c) uniform RVB and (g) U(1) Dirac QSLs, the spin-up and -down bands of spinons are degenerate in zero field [the flat band marked in blue is fourfold degenerate in (g)] and are split in an applied magnetic field [the flat bands marked in red are still doubly degenerate in (g)]. In the case of $\mathbb{Z}_2[0, \pi]\beta$ state (k), the applied field shifts the energy levels up by $\mu_0 H_\parallel \mu_{\rm eff}$. (d), (h), (l) Low-$T$ specific heat of YCOB measured in magnetic fields applied along the c axis, with colored lines showing the calculations using the mean-field ansatz of uniform RVB, U(1) Dirac, and $\mathbb{Z}_2[0, \pi]\beta$ states. The solid lines display the fits with the adjustable effective magnetic moment $\mu_{\rm eff} \sim 0.5\mu_{\rm B}$, whereas the dashed lines show the results with the fixed $\mu_{\rm eff} = \mu_{\rm B}$.

1. Uniform resonating-valence-bond state

The simplest mean-field Hamiltonian is the so-called uniform RVB state and is given by [11]

$$\mathcal{H}_{\rm uniform} = -J_1[\lambda_3 \sum_{j\sigma} f^\dagger_{j\sigma} f_{j\sigma} + \chi_1 \sum_{\langle jl\rangle,\sigma} (f^\dagger_{j\sigma} f_{l\sigma} + \text{H.c.})] - \mu_0 H_\parallel \mu_{\rm eff} \sum_{j,\sigma} \sigma f^\dagger_{j\sigma} f_{j\sigma}, \quad \text{(F1)}$$

where $\sigma = \uparrow (+1)$ and $\downarrow (-1)$ represent spin-up and -down fermionic spinons, respectively, $\mu_{\rm eff}$ is the effective spin-$\frac{1}{2}$ moment, and χ_1 is the first-neighbor hopping term [see Fig. 17(a)]. The chemical potential λ_3 in both the uniform RVB and U(1) Dirac scenarios are self-consistently determined by the constraint, $\sum_j(\sum_\sigma \langle f^\dagger_{j\sigma} f_{j\sigma}\rangle - 1) = 0$, at each temperature and in each applied magnetic field [11], and $J_1 = 60$ K is fixed in this section. It is worth mentioning that the above constraint isn't strict enough to impose the single-occupancy constraint $\sum_\sigma f^\dagger_{j\sigma} f_{j\sigma} = 1$ [7]. Therefore, in the framework of the mean-field theory, many unphysical states can contribute to extra density of states and thus specific heat, which may account for the reduced specific heat coefficient γ_2 and effective magnetic moment $\mu_{\rm eff}$ observed in YCOB (see below).

Below $\sim$1 K, the zero-field specific heat of YCOB exhibits a nearly quadratic temperature dependence, $C_{\rm p} = 0.142(1)T^{2.31(1)}$ (JK^{-1}/mol-Cu), which contradicts the uniform RVB state. A linear temperature dependence of specific heat is expected in the uniform RVB state because of the large Fermi surface [see Fig. 17(c)]. The applied magnetic field up

to ∼6 T only slightly changes the density of states around the Fermi surface, and thus the calculated field dependence of specific heat is extremely weak [see Fig. 17(d)]. In contrast, the specific heat measured on YCOB shows a clear magnetic-field dependence [see Fig. 17(d)] and thus unambiguously precludes the uniform RVB scenario.

2. U(1) Dirac spin liquid

Similarly, the mean-field ansatz of the U(1) SL state is given by [11]

$$\mathcal{H}_{\mathrm{U(1)}} = -J_1\left[\lambda_3\sum_{j,\sigma} f^\dagger_{j\sigma}f_{j\sigma} + \chi_1\sum_{\langle jl\rangle,\sigma}\nu_{jl}(f^\dagger_{j\sigma}f_{l\sigma} + \mathrm{H.c.})\right] - \mu_0 H_\parallel \mu_{\mathrm{eff}}\sum_{j,\sigma}\sigma f^\dagger_{j\sigma}f_{j\sigma}, \tag{F2}$$

where $\nu_{jl} \equiv \pm 1$ presents the sign structure of hopping terms [see Fig. 17(e)]. Our calculated band structure is identical to that reported in Ref. [11], and the temperature and field dependence of low-T specific heat in both $\mu_0 H_\parallel \mu_{\mathrm{eff}} \ll k_{\mathrm{B}}T \ll \chi_1 J_1$ and $k_{\mathrm{B}}T \ll \mu_0 H_\parallel \mu_{\mathrm{eff}} \ll \chi_1 J_1$ limits are reproduced.

At 0 T, the low-T specific heat of the U(1) SL state behaves as $C_{\mathrm{p}} = \frac{72\zeta(3)\pi k_{\mathrm{B}}^3 A}{(2\pi\hbar v_{\mathrm{F}})}T^2$ (JK^{-1}/mol-Cu) [11], where $v_{\mathrm{F}} = \frac{a\chi_1 J_1}{\sqrt{2}\hbar}$ is the Fermi velocity and $A = \frac{\sqrt{3}N_{\mathrm{A}}a^2}{6} = 7.72\times10^4$ m^2/mol-Cu is the area of the two-dimensional system. From fitting the specific heat using the quadratic-temperature function below ∼1 K, we obtain $C_{\mathrm{p}} \sim \gamma_2 T^2$ with $\gamma_2 = 0.11(1)$ JK^{-3}/mol-Cu at 0 T, and thus $v_{\mathrm{F}} = 1.07(5)\times10^3$ m/s, in YCOB. The resulting $\chi_1 = 0.29(1)$ is roughly consistent with the mean-field value of $\chi_1(\mathrm{MF}) = 0.221$ found by Hastings [64] and thus supports the U(1) Dirac scenario in YCOB. The mean-field theory gives a slightly overestimated specific heat coefficient $\gamma_2(\mathrm{MF}) = \frac{6\sqrt{3}\zeta(3)k_{\mathrm{B}}^3 N_{\mathrm{A}}}{\pi J_1^2[\chi_1(\mathrm{MF})]^2} = 0.188$ JK^{-3}/mol-Cu, possibly owing to the unphysical states (see above).

When a magnetic field is applied, the band structure tends to form Fermi pockets around the Dirac nodes in the reciprocal space [see Fig. 17(g)]. Therefore, both low-energy density of states and thus low-T specific heat increase with the strength of the magnetic field. The spinons with the free electron moment $\mu_{\mathrm{eff}} = \mu_{\mathrm{B}}$ will cause a stronger dependence of specific heat upon the magnetic field, and obviously can't explain the observations, resulting in a large $R_p = 127$ [see Fig. 17(h)]. A remedy is to set μ_{eff} to an adjustable parameter. From fitting all the low-T (<1 K) specific heat data of YCOB simultaneously, we obtain $\chi_1 = 0.27$ and a significantly reduced moment $\mu_{\mathrm{eff}} = 0.43\mu_{\mathrm{B}}$ with the least $R_p = 20.4$ [see Fig. 17(h)].

3. $\mathbb{Z}_2[0,\pi]\beta$ spin liquid

Finally, we check the $\mathbb{Z}_2$ scenario for YCOB and use the mean-field Hamiltonian previously reported in Ref. [63],

$$\mathcal{H}_{\mathbb{Z}_2} = -J_1\Bigg[\sum_j(\lambda_3\sum_\sigma f^\dagger_{j\sigma}f_{j\sigma} + \lambda_1 f^\dagger_{j\uparrow}f^\dagger_{j\downarrow} + \mathrm{H.c.}) + \chi_1\sum_{\langle jl\rangle,\sigma}\nu_{jl}(f^\dagger_{j\sigma}f_{l\sigma} + \mathrm{H.c.} + \sum_{\langle\langle jl'\rangle\rangle}\nu_{jl}(\chi_2\sum_\sigma f^\dagger_{j\sigma}f_{l'\sigma} + \Delta_2\sum_\sigma\sigma f^\dagger_{j\sigma}f^\dagger_{l'\bar{\sigma}} + \mathrm{H.c.})\Bigg] - \mu_0 H_\parallel\mu_{\mathrm{eff}}\sum_{j,\sigma}\sigma f^\dagger_{j\sigma}f_{j\sigma}, \tag{F3}$$

where λ_1 and λ_3 are single-ion chemical potentials self-consistently determined by $\sum_j\langle f^\dagger_{j\uparrow}f^\dagger_{j\downarrow}\rangle = \sum_j\langle f_{j\uparrow}f_{j\downarrow}\rangle = 0$ and $\sum_j(\sum_\sigma\langle f^\dagger_{j\sigma}f_{j\sigma}\rangle - 1) = 0$, and the mean-field ansatz up to the second neighbors in a unit cell is shown in Fig. 17(i). By setting the mean-field parameters $\chi_2 = \Delta_2 = 0$, we naturally go back to the U(1) Dirac scenario [see Eq. (F2)] and reproduce the band structure [85] and observable quantities (e.g., specific heat) of the U(1) Dirac QSL. When both χ_2 and Δ_2 are small, the $\mathbb{Z}_2[0,\pi]\beta$ state is in the neighborhood of the U(1) Dirac SL state, and has a small gap due to the singlet-pairing term $\Delta_2 \neq 0$ around the wave vectors of the previous U(1) Dirac nodes.

Similarly, from fitting the specific heat data below ∼1 K, we obtain $\chi_1 = 0.176$, $\chi_2 = 0.043$, $\Delta_2 = 0.013$, and $\mu_{\mathrm{eff}} = 0.48\mu_{\mathrm{B}}$ with the least $R_p = 7.9$ [see Fig. 17(l)]. The Δ_2 term opens a small spin (triplet) gap $\sim 0.14\chi_1 J_1 \sim 0.025 J_1$ in the band structure [see Fig. 17(k)]. When $\mu_{\mathrm{eff}} = \mu_{\mathrm{B}}$ is fixed, we get $\chi_1 = 0.160$, $\chi_2 = 0.11$, and $\Delta_2 = 0.014$, with $R_p = 32.4$ [see Fig. 17(l)].

[1] P. W. Anderson, Resonating valence bonds: A new kind of insulator? Mater. Res. Bull. **8**, 153 (1973).

[2] C. Nayak, S. H. Simon, A. Stern, M. Freedman, and S. Das Sarma, Non-Abelian anyons and topological quantum computation, Rev. Mod. Phys. **80**, 1083 (2008).

[3] P. W. Anderson, The resonating valence bond state in La_2CuO_4 and superconductivity, Science **235**, 1196 (1987).

[4] Y. Kasahara, T. Ohnishi, Y. Mizukami, O. Tanaka, S. Ma, K. Sugii, N. Kurita, H. Tanaka, J. Nasu, Y. Motome, T. Shibauchi, and Y. Matsuda, Majorana quantization and half-integer thermal quantum Hall effect in a Kitaev spin liquid, Nature (London) **559**, 227 (2018).

[5] L. Balents, Spin liquids in frustrated magnets, Nature (London) **464**, 199 (2010).

[6] C. Broholm, R. J. Cava, S. A. Kivelson, D. G. Nocera, M. R. Norman, and T. Senthil, Quantum spin liquids, Science **367**, eaay0668 (2020).

[7] Y. Zhou, K. Kanoda, and T.-K. Ng, Quantum spin liquid states, Rev. Mod. Phys. **89**, 025003 (2017).

[8] Y. Li, $YbMgGaO_4$: A Triangular-Lattice Quantum Spin Liquid Candidate, Adv. Quantum Technol. **2**, 1900089 (2019).

[9] V. Elser, Nuclear Antiferromagnetism in a Registered ^{3}He Solid, Phys. Rev. Lett. **62**, 2405 (1989).

[10] C. Waldtmann, H.-U. Everts, B. Bernu, C. Lhuillier, P. Sindzingre, P. Lecheminant, and L. Pierre, First excitations of

the spin 1/2 Heisenberg antiferromagnet on the kagomé lattice, Eur. Phys. J. B **2**, 501 (1998).

[11] Y. Ran, M. Hermele, P. A. Lee, and X.-G. Wen, Projected-Wave-Function Study of the Spin-1/2 Heisenberg Model on the Kagomé Lattice, Phys. Rev. Lett. **98**, 117205 (2007).

[12] H. J. Liao, Z. Y. Xie, J. Chen, Z. Y. Liu, H. D. Xie, R. Z. Huang, B. Normand, and T. Xiang, Gapless Spin-Liquid Ground State in the $S = 1/2$ Kagome Antiferromagnet, Phys. Rev. Lett. **118**, 137202 (2017).

[13] Y.-C. He, M. P. Zaletel, M. Oshikawa, and F. Pollmann, Signatures of Dirac Cones in a DMRG Study of the Kagome Heisenberg Model, Phys. Rev. X **7**, 031020 (2017).

[14] W. Zhu, X. Chen, Y.-C. He, and W. Witczak-Krempa, Entanglement signatures of emergent Dirac fermions: Kagome spin liquid and quantum criticality, Sci. Adv. **4**, eaat5535 (2018).

[15] C.-Y. Lee, B. Normand, and Y.-J. Kao, Gapless spin liquid in the kagome Heisenberg antiferromagnet with Dzyaloshinskii-Moriya interactions, Phys. Rev. B **98**, 224414 (2018).

[16] S. Yan, D. A. Huse, and S. R. White, Spin-liquid ground state of the $S = 1/2$ kagome Heisenberg antiferromagnet, Science **332**, 1173 (2011).

[17] S. Depenbrock, I. P. McCulloch, and U. Schollwöck, Nature of the Spin-Liquid Ground State of the $S = 1/2$ Heisenberg Model on the Kagome Lattice, Phys. Rev. Lett. **109**, 067201 (2012).

[18] Y. Iqbal, F. Becca, S. Sorella, and D. Poilblanc, Gapless spin-liquid phase in the kagome spin-$\frac{1}{2}$ Heisenberg antiferromagnet, Phys. Rev. B **87**, 060405(R) (2013).

[19] Y. Iqbal, D. Poilblanc, and F. Becca, Vanishing spin gap in a competing spin-liquid phase in the kagome Heisenberg antiferromagnet, Phys. Rev. B **89**, 020407(R) (2014).

[20] M. P. Shores, E. A. Nytko, B. M. Bartlett, and D. G. Nocera, A structurally perfect $S = 1/2$ kagomé antiferromagnet, J. Am. Chem. Soc. **127**, 13462 (2005).

[21] J. S. Helton, K. Matan, M. P. Shores, E. A. Nytko, B. M. Bartlett, Y. Yoshida, Y. Takano, A. Suslov, Y. Qiu, J.-H. Chung, D. G. Nocera, and Y. S. Lee, Spin Dynamics of the Spin-1/2 Kagome Lattice Antiferromagnet $ZnCu_3(OH)_6Cl_2$, Phys. Rev. Lett. **98**, 107204 (2007).

[22] F. Bert, S. Nakamae, F. Ladieu, D. L'Hôte, P. Bonville, F. Duc, J.-C. Trombe, and P. Mendels, Low temperature magnetization of the $S = \frac{1}{2}$ kagome antiferromagnet $ZnCu_3(OH)_6Cl_2$, Phys. Rev. B **76**, 132411 (2007).

[23] M. A. de Vries, K. V. Kamenev, W. A. Kockelmann, J. Sanchez-Benitez, and A. Harrison, Magnetic Ground State of an Experimental $S = 1/2$ Kagome Antiferromagnet, Phys. Rev. Lett. **100**, 157205 (2008).

[24] T.-H. Han, J. S. Helton, S. Chu, D. G. Nocera, J. A. Rodriguez-Rivera, C. Broholm, and Y. S. Lee, Fractionalized excitations in the spin-liquid state of a kagome-lattice antiferromagnet, Nature (London) **492**, 406 (2012).

[25] T.-H. Han, M. R. Norman, J.-J. Wen, J. A. Rodriguez-Rivera, J. S. Helton, C. Broholm, and Y. S. Lee, Correlated impurities and intrinsic spin-liquid physics in the kagome material herbertsmithite, Phys. Rev. B **94**, 060409(R) (2016).

[26] A. Olariu, P. Mendels, F. Bert, F. Duc, J. C. Trombe, M. A. de Vries, and A. Harrison, ^{17}O NMR Study of the Intrinsic Magnetic Susceptibility and Spin Dynamics of the Quantum Kagome Antiferromagnet $ZnCu_3(OH)_6Cl_2$, Phys. Rev. Lett. **100**, 087202 (2008).

[27] M. Fu, T. Imai, T.-H. Han, and Y. S. Lee, Evidence for a gapped spin-liquid ground state in a kagome Heisenberg antiferromagnet, Science **350**, 655 (2015).

[28] P. Khuntia, M. Velazquez, Q. Barthélemy, F. Bert, E. Kermarrec, A. Legros, B. Bernu, L. Messio, A. Zorko, and P. Mendels, Gapless ground state in the archetypal quantum kagome antiferromagnet $ZnCu_3(OH)_6Cl_2$, Nat. Phys. **16**, 469 (2020).

[29] B. Fåk, E. Kermarrec, L. Messio, B. Bernu, C. Lhuillier, F. Bert, P. Mendels, B. Koteswararao, F. Bouquet, J. Ollivier, A. D. Hillier, A. Amato, R. H. Colman, and A. S. Wills, Kapellasite: A Kagome Quantum Spin Liquid with Competing Interactions, Phys. Rev. Lett. **109**, 037208 (2012).

[30] E. Kermarrec, A. Zorko, F. Bert, R. H. Colman, B. Koteswararao, F. Bouquet, P. Bonville, A. Hillier, A. Amato, J. van Tol, A. Ozarowski, A. S. Wills, and P. Mendels, Spin dynamics and disorder effects in the $S = \frac{1}{2}$ kagome Heisenberg spin-liquid phase of kapellasite, Phys. Rev. B **90**, 205103 (2014).

[31] Z. Feng, Z. Li, X. Meng, W. Yi, Y. Wei, J. Zhang, Y.-C. Wang, W. Jiang, Z. Liu, and S. Li, Gapped spin-1/2 spinon excitations in a new kagome quantum spin liquid compound $Cu_3Zn(OH)_6FBr$, Chin. Phys. Lett. **34**, 077502 (2017).

[32] Y. Fu, M.-L. Lin, L. Wang, Q. Liu, L. Huang, W. Jiang, Z. Hao, C. Liu, H. Zhang, X. Shi, J. Zhang, J. Dai, D. Yu, F. Ye, P. A. Lee, P.-H. Tan, and J.-W. Mei, Dynamic fingerprint of fractionalized excitations in single-crystalline $Cu_3Zn(OH)_6FBr$, Nat. Commun. **12**, 3048 (2021).

[33] F. H. Aidoudi, D. W. Aldous, R. J. Goff, A. M. Z. Slawin, J. Paul Attfield, R. E. Morris, and P. Lightfoot, An ionothermally prepared $S = 1/2$ vanadium oxyfluoride kagome lattice, Nat. Chem. **3**, 801 (2011).

[34] L. Clark, J. C. Orain, F. Bert, M. A. De Vries, F. H. Aidoudi, R. E. Morris, P. Lightfoot, J. S. Lord, M. T. F. Telling, P. Bonville, J. P. Attfield, P. Mendels, and A. Harrison, Gapless Spin Liquid Ground State in the $S = 1/2$ Vanadium Oxyfluoride Kagome Antiferromagnet $[NH_4]_2[C_7H_{14}N][V_7O_6F_{18}]$, Phys. Rev. Lett. **110**, 207208 (2013).

[35] N. Jiang, A. Ramanathan, J. Bacsa, and H. S. L. Pierre, Synthesis of a d^1-titanium fluoride kagome lattice antiferromagnet, Nat. Chem. **12**, 691 (2020).

[36] Y. Li, B. Pan, S. Li, W. Tong, L. Ling, Z. Yang, J. Wang, Z. Chen, Z. Wu, and Q. Zhang, Gapless quantum spin liquid in the $S = 1/2$ anisotropic kagome antiferromagnet $ZnCu_3(OH)_6SO_4$, New J. Phys. **16**, 93011 (2014).

[37] M. Gomilšek, M. Klanjšek, R. Žitko, M. Pregelj, F. Bert, P. Mendels, Y. Li, Q. M. Zhang, and A. Zorko, Field-Induced Instability of a Gapless Spin Liquid with a Spinon Fermi Surface, Phys. Rev. Lett. **119**, 137205 (2017).

[38] M. Gomilšek, R. Žitko, M. Klanjšek, M. Pregelj, C. Baines, Y. Li, Q. M. Zhang, and A. Zorko, Kondo screening in a charge-insulating spinon metal, Nat. Phys. **15**, 754 (2019).

[39] M. R. Norman, Colloquium: Herbertsmithite and the search for the quantum spin liquid, Rev. Mod. Phys. **88**, 041002 (2016).

[40] X.-H. Chen, Y.-X. Huang, Y. Pan, and J.-X. Mi, Quantum spin liquid candidate $YCu_3(OH)_6Br_2[Br_x(OH)_{1-x}]$ ($x \approx 0.51$): With an almost perfect kagomé layer, J. Magn. Magn. Mater. **512**, 167066 (2020).

[41] Z. Zeng, X. Ma, S. Wu, H.-F. Li, Z. Tao, X. Lu, X.-h. Chen, J.-X. Mi, S. Song, G. Cao, G. Che, K. Li, G. Li, H. Luo, Z. Y. Meng, and S. Li, Possible dirac quantum spin liquid in a kagome quantum antiferromagnet $YCu_3(OH)_6Br_2[Br_x(OH)_{1-x}]$, arXiv:2107.11942.

[42] The Schottky anomaly of the H and D nuclear spins can appear in C_p below ∼0.2 K [36,41,86], and the temperature of 0.36 K ∼$0.006J_1$ is low enough for YCOB that the entropy flattens out at $S_m < 1.3\%R\ln 2$ [see Fig. 15(d)].

[43] G. Kresse and J. Furthmüller, Efficiency of ab-initio total energy calculations for metals and semiconductors using a plane-wave basis set, Comput. Mater. Sci. **6**, 15 (1996).

[44] G. Kresse and J. Furthmüller, Efficient iterative schemes for ab initio total-energy calculations using a plane-wave basis set, Phys. Rev. B **54**, 11169 (1996).

[45] Because the ideal NN KHA exhibits a broad peak in susceptibility at $T_p \sim 0.154J_1 \sim 9$ K.

[46] A. Zorko, S. Nellutla, J. van Tol, L. C. Brunel, F. Bert, F. Duc, J.-C. Trombe, M. A. de Vries, A. Harrison, and P. Mendels, Dzyaloshinsky-Moriya Anisotropy in the Spin-1/2 Kagome Compound $ZnCu_3(OH)_6Cl_2$, Phys. Rev. Lett. **101**, 026405 (2008).

[47] T. Arh, M. Gomilšek, P. Prelovšek, M. Pregelj, M. Klanjšek, A. Ozarowski, S. J. Clark, T. Lancaster, W. Sun, J.-X. Mi, and A. Zorko, Origin of Magnetic Ordering in a Structurally Perfect Quantum Kagome Antiferromagnet, Phys. Rev. Lett. **125**, 027203 (2020).

[48] T. Li, A continuous family of fully frustrated Heisenberg models on the kagome lattice, Europhys. Lett. **133**, 47001 (2021).

[49] T. Han, S. Chu, and Y. S. Lee, Refining the Spin Hamiltonian in the spin-$\frac{1}{2}$ Kagome Lattice Antiferromagnet $ZnCu_3(OH)_6Cl_2$ Using Single Crystals, Phys. Rev. Lett. **108**, 157202 (2012).

[50] J. Schnack, J. Schulenburg, and J. Richter, Magnetism of the $N = 42$ kagome lattice antiferromagnet, Phys. Rev. B **98**, 094423 (2018).

[51] Y. Mizuno, T. Tohyama, S. Maekawa, T. Osafune, N. Motoyama, H. Eisaki, and S. Uchida, Electronic states and magnetic properties of edge-sharing Cu-O chains, Phys. Rev. B **57**, 5326 (1998).

[52] Y. Li, S. Bachus, H. Deng, W. Schmidt, H. Thoma, V. Hutanu, Y. Tokiwa, A. A. Tsirlin, and P. Gegenwart, Partial Up-Up-Down Order with the Continuously Distributed Order Parameter in the Triangular Antiferromagnet $TmMgGaO_4$, Phys. Rev. X **10**, 011007 (2020).

[53] Y. Li, Q.-Y. Li, W. Li, T. Liu, D. J. Voneshen, P. K. Biswas, and D. Adroja, Spin dynamics and Griffiths singularity in the random quantum Ising magnet $PrTiNbO_6$, npj Quantum Mater. **6**, 34 (2021).

[54] H. Kawamura, K. Watanabe, and T. Shimokawa, Quantum spin-liquid behavior in the spin-1/2 random-bond Heisenberg antiferromagnet on the kagome lattice, J. Phys. Soc. Jpn. **83**, 103704 (2014).

[55] K. Gregor and O. I. Motrunich, Nonmagnetic impurities in the spin-1/2 kagome antiferromagnet, Phys. Rev. B **77**, 184423 (2008).

[56] I. Rousochatzakis, S. R. Manmana, A. M. Läuchli, B. Normand, and F. Mila, Dzyaloshinskii-Moriya anisotropy and nonmagnetic impurities in the $s = \frac{1}{2}$ kagome system $ZnCu_3(OH)_6Cl_2$, Phys. Rev. B **79**, 214415 (2009).

[57] R. R. P. Singh, Valence Bond Glass Phase in Dilute Kagome Antiferromagnets, Phys. Rev. Lett. **104**, 177203 (2010).

[58] T. Shimokawa, K. Watanabe, and H. Kawamura, Static and dynamical spin correlations of the $S = \frac{1}{2}$ random-bond antiferromagnetic Heisenberg model on the triangular and kagome lattices, Phys. Rev. B **92**, 134407 (2015).

[59] K. Watanabe, H. Kawamura, H. Nakano, and T. Sakai, Quantum spin-liquid behavior in the spin-1/2 random Heisenberg antiferromagnet on the triangular lattice, J. Phys. Soc. Jpn. **83**, 034714 (2014).

[60] I. Kimchi, J. P. Sheckelton, T. M. Mcqueen, and P. A. Lee, Scaling and data collapse from local moments in frustrated disordered quantum spin systems, Nat. Commun. **9**, 4367 (2018).

[61] X. Hong, M. Behnami, L. Yuan, B. Li, W. Brenig, B. Büchner, Y. Li, and C. Hess, Thermal conductivity of the kagome Heisenberg antiferromagnet $YCu_3(OH)_{6.5}Br_{2.5}$ (unpublished).

[62] X.-G. Wen, Quantum orders and symmetric spin liquids, Phys. Rev. B **65**, 165113 (2002).

[63] Y.-M. Lu, Y. Ran, and P. A. Lee, $\mathbb{Z}_2$ spin liquids in the $S = \frac{1}{2}$ Heisenberg model on the kagome lattice: A projective symmetry-group study of Schwinger fermion mean-field states, Phys. Rev. B **83**, 224413 (2011).

[64] M. B. Hastings, Dirac structure, RVB, and Goldstone modes in the kagomé antiferromagnet, Phys. Rev. B **63**, 014413 (2000).

[65] O. I. Motrunich, Variational study of triangular lattice spin-$\frac{1}{2}$ model with ring exchanges and spin liquid state in $\kappa-(ET)_2Cu_2(CN)_3$, Phys. Rev. B **72**, 045105 (2005).

[66] The significant decrease of the effective magnetic moment from μ_B may originate from the unphysical states due to the rough treatment of the single-occupied condition, which is another issue beyond the mean-field theory worth of further research.

[67] W. Sun, Y.-X. Huang, S. Nokhrin, Y. Pan, and J.-X. Mi, Perfect kagome lattices in $YCu_3(OH)_6Cl_3$: A new candidate for the quantum spin liquid state, J. Mater. Chem. C **4**, 8772 (2016).

[68] Q. Barthélemy, P. Puphal, K. M. Zoch, C. Krellner, H. Luetkens, C. Baines, D. Sheptyakov, E. Kermarrec, P. Mendels, and F. Bert, Local study of the insulating quantum kagome antiferromagnets $YCu_3(OH)_6O_xCl_{3-x}$ ($x = 0$, 1/3), Phys. Rev. Mater. **3**, 074401 (2019).

[69] A. Zorko, M. Pregelj, M. Klanjšek, M. Gomilšek, Z. Jagličič, J. S. Lord, J. A. T. Verezhak, T. Shang, W. Sun, and J. X. Mi, Coexistence of magnetic order and persistent spin dynamics in a quantum kagome antiferromagnet with no intersite mixing, Phys. Rev. B **99**, 214441 (2019).

[70] A. Zorko, M. Pregelj, M. Gomilšek, M. Klanjšek, O. Zaharko, W. Sun, and J. X. Mi, Negative-vector-chirality 120° spin structure in the defect- and distortion-free quantum kagome antiferromagnet $YCu_3(OH)_6Cl_3$, Phys. Rev. B **100**, 144420 (2019).

[71] Z. Zhu, P. A. Maksimov, S. R. White, and A. L. Chernyshev, Disorder-Induced Mimicry of a Spin Liquid in $YbMgGaO_4$, Phys. Rev. Lett. **119**, 157201 (2017).

[72] I. Kimchi, A. Nahum, and T. Senthil, Valence Bonds in Random Quantum Magnets: Theory and Application to $YbMgGaO_4$, Phys. Rev. X **8**, 031028 (2018).

[73] A. Abragam and B. Bleaney, *Electron Paramagnetic Resonance of Transition Ions* (Oxford University Press, Oxford, 2012).

[74] M. Valko, P. Pelikán, S. Biskupič, and M. Mazúr, ESR spectra of copper-(II) complexes in the solids, Chem. Papers **44**, 805 (1990).

[75] J. Liu, B. Liu, L. Yuan, B. Li, L. Xie, X. Chen, H. Zhang, D. Xu, W. Tong, J. Wang, and Y. Li, Frustrated magnetism of the triangular-lattice antiferromagnets α-CrOOH and α-CrOOD, New J. Phys. **23**, 033040 (2021).

[76] O. Janson, S. Furukawa, T. Momoi, P. Sindzingre, J. Richter, and K. Held, Magnetic Behavior of Volborthite $Cu_3V_2O_7(OH)_2\cdot 2H_2O$ Determined by Coupled Trimers Rather Than Frustrated Chains, Phys. Rev. Lett. **117**, 037206 (2016).

[77] O. Janson, J. Richter, and H. Rosner, Modified Kagome Physics in the Natural Spin-1/2 Kagome Lattice Systems: Kapellasite $Cu_3Zn(OH)_6Cl_2$ and Haydeeite $Cu_3Mg(OH)_6Cl_2$, Phys. Rev. Lett. **101**, 106403 (2008).

[78] Y. Li, D. Adroja, R. I. Bewley, D. Voneshen, A. A. Tsirlin, P. Gegenwart, and Q. Zhang, Crystalline Electric-Field Randomness in the Triangular Lattice Spin-Liquid $YbMgGaO_4$, Phys. Rev. Lett. **118**, 107202 (2017).

[79] J. P. Perdew, K. Burke, and M. Ernzerhof, Generalized gradient approximation made simple, Phys. Rev. Lett. **77**, 3865 (1996).

[80] The main changes are the increases of the fitted J_1 and least R_p by $\sim$2 K and $\sim$0.6, respectively, after the subtraction.

[81] G. Misguich and P. Sindzingre, Magnetic susceptibility and specific heat of the spin-$\frac{1}{2}$ Heisenberg model on the kagome lattice and experimental data on $ZnCu_3(OH)_6Cl_2$, Eur. Phys. J. B **59**, 305 (2007).

[82] J. Jaklič and P. Prelovšek, Lanczos method for the calculation of finite-temperature quantities in correlated systems, Phys. Rev. B **49**, 5065(R) (1994).

[83] Y. Li, H. Liao, Z. Zhang, S. Li, F. Jin, L. Ling, L. Zhang, Y. Zou, L. Pi, Z. Yang, J. Wang, Z. Wu, and Q. Zhang, Gapless quantum spin liquid ground state in the two-dimensional spin-1/2 triangular antiferromagnet $YbMgGaO_4$, Sci. Rep. **5**, 16419 (2015).

[84] Y. Li, S. Bachus, Y. Tokiwa, A. A. Tsirlin, and P. Gegenwart, Gapped ground state in the zigzag pseudospin-1/2 quantum antiferromagnetic chain compound $PrTiNbO_6$, Phys. Rev. B **97**, 184434 (2018).

[85] It is worth mentioning that there is a flip for the spin-down band since we use the Nambu representation in the $\mathbb{Z}_2[0,\pi]\beta$ scenario.

[86] S. Yamashita, T. Yamamoto, Y. Nakazawa, M. Tamura, and R. Kato, Gapless spin liquid of an organic triangular compound evidenced by thermodynamic measurements, Nat. Commun. **2**, 275 (2011).